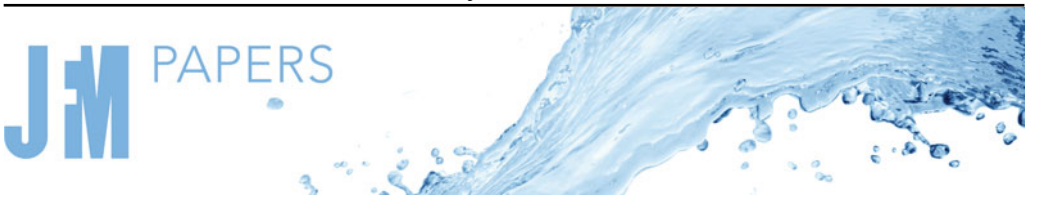
J. Fluid Mech. (2026), *vol.* 1046, A65, doi:10.1017/jfm.2026.12248



Shock-wave–boundary-layer interaction over an axisymmetric body

Anirudh Lakshmi Narasimha Prasad[1], **Niyati Chokshi**[2] **and S. Unnikrishnan**[2]

[1]Department of Mechanical and Aerospace Engineering, University of Colorado, Colorado Springs, CO 80918, USA

[2]Department of Mechanical and Aerospace Engineering, FAMU-FSU College of Engineering, Florida State University, Tallahassee, FL 32310, USA

Corresponding author: Anirudh Lakshmi Narasimha Prasad, alakshmi@uccs.edu

(Received 19 August 2025 UTC; revised 6 August 2026 UTC; accepted 3 October 2026 UTC)

This study investigates the flow topology and unsteadiness induced by the interaction of an oblique shock and a supersonic boundary layer developing over an axisymmetric body, using implicit large-eddy simulations. The interaction produces highly three-dimensional flow features, including an open separation region, multiple vortex pairs and strong cross-flow, influenced by the surface curvature and the strong adverse pressure gradient. Three major vortex systems are identified: a primary vortex that detaches from the surface, a secondary vortex near the surface that dominates unsteadiness and a weaker tertiary vortex that dissipates downstream. Turbulence generation mechanisms vary in the azimuthal direction, with production being the dominant source on the windward plane, while turbulent transport contributes mostly in the leeward wake. Windward side unsteady dynamics is dominated by four major frequency bands: a very-low-frequency band ($St_L \sim 0.03$, where St is Strouhal number, St_L is the Strouhal number with length of separation bubble as reference length) associated with bubble breathing, low-frequency shear-layer flapping at $St_L \sim 0.1$, Kelvin–Helmholtz shedding in the shear layer at $St_L \sim 1$ and high-frequency content corresponding to fine-scale convection in the boundary layer. Leeward side dynamics is influenced by the coherent structures generated in the secondary and tertiary vortex pairs, resulting from short-wavelength elliptic instability, leading to vortex meandering. The primary vortex displays a 'V'-shaped vertical oscillations corresponding to the very-low-frequency band, highlighting the impact of shock-wave/boundary-layer interaction bubble breathing on large-scale vortex oscillations. This low-frequency vortex dynamics has a significant impact on the aerodynamic loading on the cylinder.

Key words: boundary layer separation, shock waves, vortex dynamics

© The Author(s), 2026. Published by Cambridge University Press. This is an Open Access article, distributed under the terms of the Creative Commons Attribution licence (https://creativecommons.org/licenses/by/4.0/), which permits unrestricted re-use, distribution and reproduction, provided the original article is properly cited.

https://doi.org/10.1017/jfm.2026.12248 Published online by Cambridge University Press

1. Introduction

Shock-wave/boundary-layer interactions (SWBLIs) play a pivotal role in influencing the aerodynamic performance, stability and safety of high-speed vehicles. The SWBLIs may induce undesirable outcomes, including heightened drag (Schülein 2006), reduced propulsion efficiency, oscillatory loadings such as buzz and unstart (Xu *et al.* 2022), diminished control surface effectiveness (Gaitonde 2015) and localised thermal loads (Dwivedi *et al.* 2019), which may jeopardise the structural integrity and overall functionality of the vehicle. Consequently, a detailed understanding of SWBLIs and the development of effective control strategies to mitigate their adverse impacts are of critical importance.

Comprehensive reviews (Green 1970; Adamson Jr & Messiter 1980; Andreopoulos *et al.* 2000; Dolling 2001; Clemens & Narayanaswamy 2014; Gaitonde 2015; Sandham 2016; Gaitonde & Adler 2023; Sabnis & Babinsky 2023; Zuo & Pirozzoli 2024) have systematically documented advances in SWBLI research, addressing both two-dimensional (e.g. flat plates and compression ramps) and three-dimensional (e.g. swept ramps, fins and cone-cylinder flares) interaction scenarios. These works also highlight the parametric sensitivities of this flow problem, including effects of shock intensity, Mach number, Reynolds number, boundary-layer (BL) state and surface geometry.

The simplest of these interactions is the two-dimensional SWBLI (2-D-SWBLI), where a distinct closed separation zone is typically formed, bounded by a separation shock and a reattachment shock, both exhibiting statistical uniformity along the spanwise direction. In spite of this apparent simplicity, 2-D-SWBLIs are dynamically rich systems that support multiscale phenomena across a broad range of spatio-temporal scales. Surface flow topology associated with these closed separation regions often reveals multiple node–saddle pairs aligned with the separation and reattachment lines (Perry & Chong 1987). The separation length (L) serves as a key scaling parameter for characterising the dominant frequency content of 2-D-SWBLIs, which can be categorised into four primary frequency bands, for example, as summarised in Adler & Gaitonde (2018):

(i) $St_L \sim 0.03$: low-frequency 'breathing' oscillations characterised by large-scale displacement of the separation shock, associated with the stability of the separated flow;
(ii) $St_L \sim 0.1$: secondary oscillations in the separation bubble;
(iii) $St_L \sim 0.5$: coherent fluctuations in the separated shear layer, encompassing vortex shedding and shock flapping. This mid-frequency band aligns with the Strouhal number representative of shear-layer instabilities;
(iv) $St_L/St_\delta \sim 5/1$: high-frequency turbulent fluctuations often convected from the upstream BL.

These bands collectively capture the intricate interplay of the separation and reattachment dynamics in 2-D-SWBLIs. Further, this spectral characterisation from the 2-D interaction is particularly useful while interpreting 3-D scenarios with relatively complex scaling behaviour.

Among the various bands of unsteadiness observed in SWBLIs, the low-frequency oscillation ($St_L \sim 0.03$) has received significant attention due to its potential detrimental effects on the airframe. Specifically, the origin and sustenance of the low-frequency unsteadiness have been examined extensively via mechanisms involving upstream and downstream influence. The upstream influence framework attributes separation shock

https://doi.org/10.1017/jfm.2026.12248 Published online by Cambridge University Press

displacement to the amplification of large-scale disturbances in the incoming BL (Poggie *et al.* 2015), with the coherent super-structures documented by Ganapathisubramani *et al.* (2009) playing a notable role. The downstream influence perspective interprets the unsteadiness as a manifestation of the oscillator dynamics within the bubble, driven by convective feedback and global instabilities (Touber & Sandham 2009; Poggie *et al.* 2015; Schmid & Sipp 2016; Nichols *et al.* 2017). Clemens & Narayanaswamy (2014) further note that strong separation is governed by global instabilities, whereas upstream forcing is more relevant for weaker separations.

In comparison with 2-D-SWBLIs, the literature on the topology and dynamics of 3-D SWBLIs (3-D-SWBLIs) is sparser. Reviews by Gaitonde & Adler (2023) and Zuo & Pirozzoli (2024) emphasise the transition from spanwise homogeneity in the former to complex 3-D flow features in 3-D cases, where scaling laws may not be apparent, and the streamlines within the recirculation region do not form closed loops. Instead, they exhibit a spiralling motion outward in the spanwise/azimuthal direction, leading to enhanced 3-D transport and mixing (Panaras 1996). Recent investigations into swept and semi-infinite configurations have revealed unique aspects of strongly swept interactions, including convective unsteadiness in the separated shear layers, contrasting with the breathing oscillations prominent in 2-D-SWBLIs (Adler & Gaitonde 2019; Seçkin *et al.* 2023). These findings demonstrate a coupling between the 2-D and 3-D shear-layer dynamics, modifying the frequency content and instability patterns of 3-D interactions.

Even less explored are SWBLIs on axisymmetric bodies (referred to as axi-SWBLIs in the following), despite their relevance to aerospace applications involving interaction of fins and control surfaces over curved fuselages, store separation scenarios and interaction of adjacent airframes in spacecraft launch configurations. Early numerical simulations (Hung 1983) and more recent experiments have documented large open separation regions (Mason *et al.* 2021) and flow topology (Wahidi *et al.* 2024) in axi-SWBLIs influenced by azimuthal effects and curvature, exhibiting low-frequency unsteadiness analogous to 2-D-SWBLIs. These open separations are characterised by the separating streamline spiralling into a focus from which flow escapes in the spanwise/azimuthal direction, forming a horseshoe vortex system (Tobak & Peake 1981; Eagle & Driscoll 2014). Experimental studies by Brosh *et al.* (1985) and Stephen *et al.* (2013) evaluated a Mach 3 axi-SWBLI and obtained oil flow visualisation that identified dual separation lines originating at the foot of the impinging shock and wrapping around the axisymmetric body. Consistent features were identified in Reynolds-averaged Navier–Stokes simulations by Bhagwandin (2015). However, the structure and development of off-surface flow structures and their role in shaping surface loading remain poorly understood.

In addition to interaction dynamics that is deviant from 2-D-SWBLIs, a unique feature of axi-SWBLIs is the strong vortex dynamics generated due to surface curvature and wake effects, which manifest as multiple coherent vortex pairs and associated instabilities. A review by Leweke *et al.* (2016) summarises various 2-D and 3-D instabilities harboured by such vortex pairs. The dominant 3-D instabilities seen in vortex pairs are the long-wavelength Crow instability (Crow 1970) and short-wave elliptic instability (Kerswell 2002). The Crow instability occurs in counter-rotating vortex pairs, appearing as a periodic sinusoidal deformation of the vortices, which is symmetric about the centre plane of the pair and inclined at approximately 45 degrees to the line connecting them. Elliptic instabilities often distort the vortex cores and are driven by parametric resonance, wherein the intrinsic oscillatory modes of a background circular flow interact with an imposed strain field (Moore & Saffman 1975; Tsai & Widnall 1976), leading to the exponential growth of 3-D perturbations, and subsequent secondary instabilities (Kerswell 1999;

https://doi.org/10.1017/jfm.2026.12248 Published online by Cambridge University Press

Sarath & Manu 2023). These instabilities are of great interest to the current study, due to their influence on the unsteady aerodynamic loading experienced by the airframe.

Considering the above, the current study is motivated by three key scientific questions:

(i) What is the nature and origin of surface and off-surface flow features observed in an axi-SWBLI?
(ii) How does open separation in an axi-SWBLI alter unsteady mechanisms from that of canonical 2-D interactions?
(iii) What is the role of the off-surface vortex dynamics in governing unsteadiness and aerodynamic loading in axi-SWBLIs?

To address these queries, the present study constitutes one of the first attempts at utilising time-resolved, 3-D high-fidelity simulations of an axi-SWBLI, combined with detailed spectral and modal analyses. The paper is organised as follows: § 2 describes the simulation set-up, including geometry and inflow conditions, with experimental comparisons presented in § 3. The mean flow topology is discussed in § 4, its influence on aerodynamic loading in § 5 and the fluctuating statistics of the interaction are presented in § 6.1. The temporal unsteadiness associated with the interaction is described in § 6.2, while the dynamics associated with the vortices is discussed in § 7.

2. Flow conditions and computational set-up

The axi-SWBLI problem is computationally studied using a laminar BL developing over a canonical cylindrical body interacting with an oblique shock. In the following, all dimensional quantities are represented using a superscript asterisk, $()^*$. The cylinder is aligned with the free stream at zero angle of attack, has a base diameter, $D^* = 25.4$ mm (1 in.), streamwise length, $h^* = 381$ mm (15 inches) and is informed by experimental data from Mason *et al.* (2021). The free-stream Mach number is $M_\infty = 2$. The oblique shock impinging on the cylinder is equivalent to that generated by a 10° wedge facing the supersonic free stream, producing a wave angle, $\beta = 39.31°$, and associated shock-induced ratios of pressure (1.70), density (1.46), temperature (1.17) and stagnation pressure (0.98). In the inviscid limit, the impingement occurs approximately 7 diameters downstream of the leading edge. The laminar BL developed over the cylinder has a mean thickness of $\delta^*_{99}/D^* \approx 0.1$, $\delta^*/D^* \approx 0.05$ and $\theta^*/D^* \approx 0.011$ prior to separation.

The computations solve the 3-D Navier–Stokes equations cast in the generalised curvilinear coordinate system, using an implicit large-eddy simulation approach, as follows:

$$\frac{\partial}{\partial \tau}\left(\frac{\boldsymbol{Q}}{J}\right) = -\left[\left(\frac{\partial \boldsymbol{F_i}}{\partial \xi} + \frac{\partial \boldsymbol{G_i}}{\partial \eta} + \frac{\partial \boldsymbol{H_i}}{\partial \zeta}\right) + \frac{1}{Re}\left(\frac{\partial \boldsymbol{F_v}}{\partial \xi} + \frac{\partial \boldsymbol{G_v}}{\partial \eta} + \frac{\partial \boldsymbol{H_v}}{\partial \zeta}\right)\right], \tag{2.1}$$

where the vector of conserved variables is $\boldsymbol{Q} = [\rho, \rho u, \rho v, \rho w, \rho E]^T$, with ρ representing the density and (u, v, w) denoting the Cartesian velocity components. The total specific internal energy, E, is given by $E = (T/\gamma(\gamma-1)M_\infty^2) + (u^2+v^2+w^2)/2$, where, T is the static temperature and γ is the ratio of specific heats. The transformation from curvilinear to Cartesian coordinates is achieved via the Jacobian, $J = \partial(\xi, \eta, \zeta, \tau)/\partial(x, y, z, t)$, where ξ, η, ζ are the spatial coordinates in curvilinear coordinate system and τ is the time in the same. The inviscid and viscous fluxes are represented by $(\boldsymbol{F_i}, \boldsymbol{G_i}, \boldsymbol{H_i})$, and $(\boldsymbol{F_v}, \boldsymbol{G_v}, \boldsymbol{H_v})$, respectively. The system of equations is closed using the ideal gas equation of state, $p = \rho T/\gamma M_\infty^2$, with a constant Prandtl

https://doi.org/10.1017/jfm.2026.12248 Published online by Cambridge University Press

number, $Pr = 0.72$. The variation of dynamic viscosity with temperature is modelled using Sutherland's law.

All primitive variables, except pressure, are non-dimensionalised by their respective free-stream values. Pressure is non-dimensionalised as $p = p^*/\rho^*_\infty u^{*2}_\infty$, where, p^* is the dimensional pressure, ρ^*_∞ is the free-stream density and u^*_∞ is the free-stream velocity. The reference length scale utilised in this study is the cylinder diameter, $D^* = 25.4$ mm (1"), and the Reynolds number is computed as $Re_D = \rho^*_\infty u^*_\infty D^*/\mu^*_\infty$, where, μ^*_∞ is the free-stream dynamic viscosity. In the present study, the axi-SWBLI is primarily evaluated at $Re_D \sim 35\,800$. Based on the BL momentum thickness prior to separation, this results in $Re_\theta = 393.80$. Time is non-dimensionalised by the characteristic time scale, $T^*_C = D^*/u^*_\infty$, with the non-dimensional time expressed as, $t = t^*/T^*_C$. The non-dimensional time step size in the computations is $\Delta t^*/T^*_C = 1 \times 10^{-3}$. The Strouhal number, which characterises the non-dimensional frequency, is defined as $St = f^* D^*/u^*_\infty$, where, f^* is the dimensional frequency in Hertz. The simulations are performed for 670 characteristic time units, with data sampled at a temporal interval corresponding to $St = 40$.

Convective fluxes are reconstructed using a seventh-order weighted essentially non-oscillatory scheme (Liu *et al.* 1994) in smooth regions, while a third-order reconstruction is utilised in the vicinity of shocks. Roe's approximate Riemann solver (Roe 1981) is employed for flux evaluation at cell interfaces. Viscous fluxes are reconstructed using fourth-order central differencing. Temporal integration is performed using the second-order diagonalised implicit Beam–Warming method (Beam & Warming 1978; Pulliam & Chaussee 1981). This solver has been validated and applied in various high-speed flow problems, including supersonic jets (Lakshmi Narasimha Prasad & Unnikrishnan 2023), high-speed BL transition (Aswathy Nair & Unnikrishnan 2024; Lakshmi Narasimha Prasad *et al.* 2025*b*) and supersonic inlets (Khobragade *et al.* 2022).

The computational domain, illustrated in figure 1, represents a 180° sector of the cylinder, comprising approximately 135×10^6 grid points. The baseline grid (that will be utilised for most of the discussion in this work) is discretised with 1501 nodes along the streamwise direction, 401 nodes along the wall-normal direction and 225 nodes along the azimuthal direction. Grid refinement is applied in the vicinity of the wall, achieving a minimum wall-normal spacing of 1×10^{-3} such that the δ_{99} value prior to separation is resolved using 97 grid points. To mitigate numerical reflections, the grid is gradually stretched towards the outflow boundaries, and the reconstruction is progressively changed from seventh order to first order. To ensure accuracy of key predictions, including location of transition, extent of separation, unsteadiness levels and vortex topology, a grid sensitivity study is also performed using a relatively finer grid, as discussed in the Appendix.

Dirichlet boundary condition (BCs) are imposed at the inflow plane to enforce free-stream conditions on the primitive variables, while zero-gradient outflow conditions are applied at the downstream outflow boundaries. Along the outer boundary, Dirichlet conditions are imposed everywhere upstream of the imposed shock and up to around one diameter downstream of the discontinuity. Beyond this, zero-gradient outflow conditions are utilised in the post-shock region to minimise boundary reflections. The jump conditions across the oblique shock are obtained using the Rankine–Hugoniot relations, which provide the post-shock properties, including pressure, density and velocity, based on the free-stream conditions and wedge angle. Symmetry BCs are enforced on the windward and leeward azimuthal faces of the 180° sector, with adiabatic no-slip conditions applied at the wall. The flow field is initialised with the ideal 1-D inviscid conditions, which cause the oblique shock to impinge on the cylinder surface at $x \sim 7$. Figure 1 also illustrates the convention adopted for referencing the azimuthal planes. The windward side is designated

https://doi.org/10.1017/jfm.2026.12248 Published online by Cambridge University Press

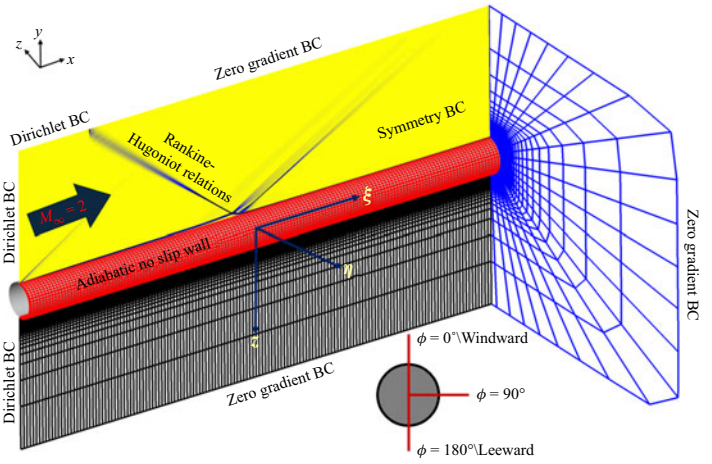


Figure 1. Computational domain and grid used for the current study. Every tenth point is shown. BCs used in the simulations are also shown. Nomenclature used to refer to various azimuthal planes is shown in the inset image.

by $\phi = 0°$, while the leeward side corresponds to $\phi = 180°$, consistent with the convention followed by Mason *et al.* (2021).

3. Experimental comparisons

In the interest of computational feasibility and providing clarity on fundamental topology and unsteadiness in axi-SWBLIs, the present work adopts several simplifications as follows, compared with the experimental campaign (Mason *et al.* 2021). While the experimental set-up involves an ogive-cylinder geometry, the simulations consider a cylindrical surface with a constant diameter throughout its streamwise extent to minimise potential complications arising from streamwise curvature. The experimental Reynolds number ($Re_D \sim 904\,745$) is higher than that in the simulations ($Re_D \sim 35\,800$), leading to differences in the state of the incoming BL and interaction strength. Finally, the present simulations assume a perfectly symmetric interaction, as imposed by the BCs on the windward and leeward planes, which restricts antisymmetric modes about the symmetry plane. Despite these differences, the experimental comparison provides an opportunity to verify whether the qualitative trends observed in the simulations are consistent with flow physics reported in the literature.

Being a non-homogeneous interaction, the axi-SWBLI engenders complex flow features, both viscous and inviscid, due to the curvature associated with the interaction surface. An overview of key flow features is first presented in figure 2, using an instantaneous visualisation of the flow field. The incident shock wraps around the azimuth of the cylinder and gets reflected as a conical shock that approaches the leeward wake as the flow develops in the streamwise direction. The separated flow arising from the adverse pressure gradient induced by the incident shock forms two distinct vortex pairs. The primary vortex pair detaches from the surface and traverses away from the cylinder on the leeward side. The secondary vortex pair remains briefly attached to the leeward side of the cylinder before detaching at a downstream location. Shear-layer instabilities develop and amplify over these coherent streamwise-oriented vortex structures, eventually disintegrating them into a turbulent wake.

https://doi.org/10.1017/jfm.2026.12248 Published online by Cambridge University Press

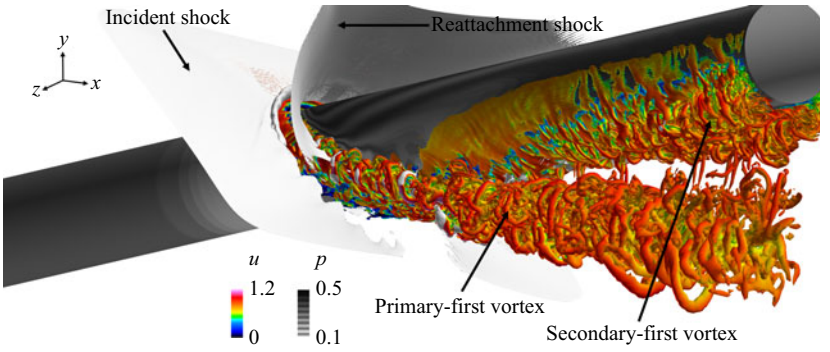


Figure 2. Instantaneous flow field of the axi-SWBLI. Vortical structures are shown via isosurfaces of unity Q-criterion coloured by streamwise velocity. Inviscid flow features are shown via isosurfaces of unity $|\nabla p|$. Contour levels on the surface of the cylinder depict wall pressure.

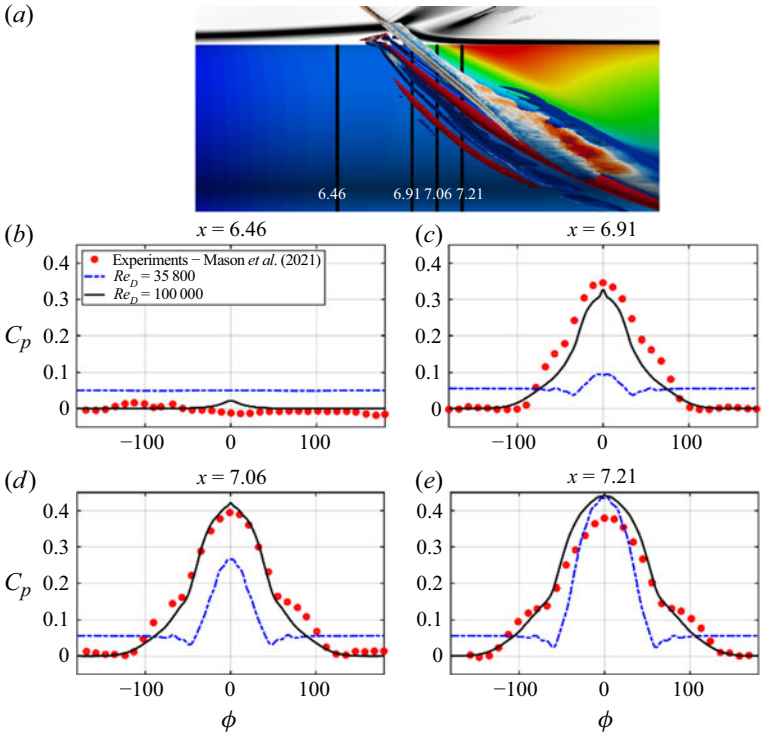


Figure 3. (a) Schematic showing the location of various streamwise locations (marked by solid black line) at which the wall pressure coefficient is compared. Azimuthal variation of wall pressure coefficient comparison between experimental data and current simulations at four streamwise locations: (b) $x = 6.46$, (c) $x = 6.91$, (d) $x = 7.06$ and (e) $x = 7.21$.

Figure 3(b,c,d,e) illustrates the azimuthal variation of the wall pressure coefficient (C_p) at four streamwise locations ($x = 6.46$, 6.91, 7.06, 7.21). These locations are in the vicinity of the interaction zone (as marked in figure 3a), and encompass the separation region on the windward plane and the wake near the leeward plane. Along with the

https://doi.org/10.1017/jfm.2026.12248 Published online by Cambridge University Press

experimental results from Mason *et al.* (2021), two simulations at $Re_D \sim 35\,800$ and $Re_D \sim 100\,000$ are included, for reasons described below. The low-Re_D simulation has a laminar BL upstream of the interaction and is the focus of this study, due to its relatively well-defined spatio-temporal dynamics, offering detailed comparisons with 2-D-SWBLIs. Further, it provides a clear depiction of the primary and secondary flow features, as well as the surface topology, associated with this non-homogeneous interaction. However, some deviations from experiments include the steady nature of the incoming BL and its enhanced proclivity to separation and upstream influence. To reconcile these differences and test the hypothesis about the Reynolds number influence, another simulation at $Re_D \sim 100\,000$ is performed with a fully turbulised incoming BL by introducing a digital-filter-based synthetic turbulence generator (Adler *et al.* 2018) at the inflow. In this case, the BL prior to separation ($x = 6$) has a thickness of $\delta^*_{99}/D^* = 0.09$, $\delta^*/D^* = 0.026$ and $\theta^*/D^* = 0.0077$, resulting in a Reynolds number of $Re_\theta = 770$. The results presented here indicate that the $Re_D \sim 100\,000$ interaction improves the comparison with the experiment.

Upstream of the shock impingement, as shown in figure 3(*b*), the low-Re_D interaction indicates slightly higher values of C_p, due to the separated state of the BL. Values from the high-Re_D simulation are closer to the experimental observations. In the interaction region (figures 3*c* and 3*d*) and downstream of the shock impingement (figure 3*e*), the pressure rise observed in the experiments closely matches the predictions of the high-Re_D simulation. While the low-Re_D simulation shows differences in peak C_p values, the overall trends in azimuthal variation are reasonably reproduced. This suggests that, as the Reynolds number and inflow conditions approach the experimental value, the simulations align more closely with experimental observations, demonstrating their accuracy and reliability.

Despite differences in the Reynolds number and the state of the incoming BL, key features of surface flow topology observed in the experiments are captured in the low-Re_D simulations, as demonstrated in figure 4. It compares experimental surface oil flow visualisations (*a–d*) with surface-constrained streamlines from the low-Re_D simulations (*e–h*) and the high-Re_D simulations (*i–l*), coloured by streamwise velocity. Features of interest are marked by the solid white line. The curved separation regions seen in figures 4(*a*,*e*) and 4(*i*) are consistently reproduced in the simulations, albeit with stronger upstream influence in the low-Re_D case. The experimental trend of increasing streamwise extent of the open separation region (figure 4*b*) as the flow develops from the windward to the leeward plane is also captured in the corresponding surface streamlines from simulations (figures 4*f* and 4*j*). The emergence of the secondary vortex pair within the open separation region, along with its meandering motion in the cylinder wake (figures 4*c* and 4*d*), are also reproduced in the computations (figures 4*g* and 4*h*, 4*k* and 4*l*). It has to be noted that the low-Re_D interaction reveals amplified and more coherent manifestations of flow features. At higher Re_D, similar features persist in a weaker and more fragmented form, with the primary and tertiary vortices undergoing the most attenuation. Further discussion on this surface flow topology is provided in the following section. Having demonstrated a qualitative agreement between the experiments and the simulations, we now present a detailed analysis of the low-Re_D interaction.

4. Interaction and wake flow fields

Flow features of the interaction and the wake are evaluated in figure 5, which shows the evolution of the shock and vortex structures on streamwise planes along the length of the cylinder, in the vicinity of the impingement location, using time-averaged contours

https://doi.org/10.1017/jfm.2026.12248 Published online by Cambridge University Press

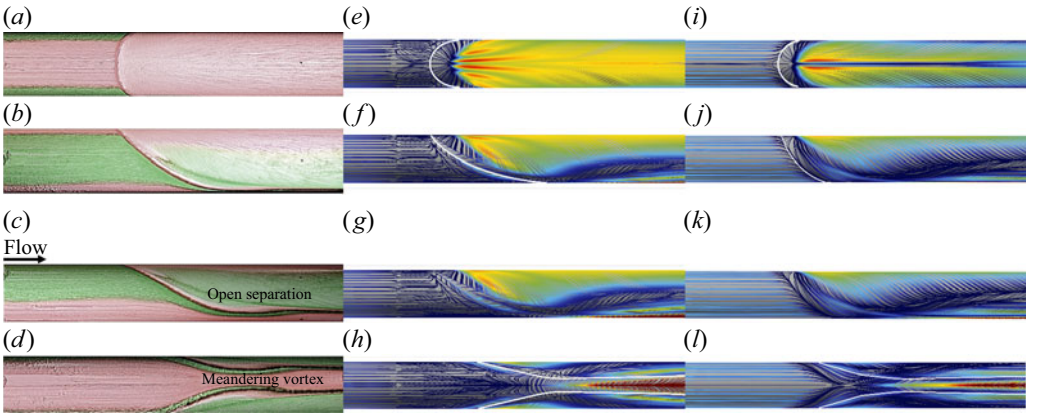


Figure 4. (*a–d*) Surface oil flow visualisation obtained from experiments. Surface-constrained streamlines coloured by streamwise velocity obtained from (*e–h*) low-Re_D simulations and (*i–l*) high-Re_D simulations. Features of interest are marked by the solid white line.

of $|\nabla\rho|$. Results from the corresponding inviscid interaction are also presented to verify current predictions with prior literature (e.g. Hung 1983), and highlight the differences caused by the presence of the separated BL and viscous effects. The left half of each panel shows the inviscid interaction, while the right half shows the viscous interaction at $Re_D \sim 35\,800$. Incident shocks of equal strength are observed at $x = 6$ in both the inviscid and viscous simulations, as shown in figure 5(*b*). As mentioned earlier, the simulations are designed such that the shock impinges on the cylinder at $x \sim 7$. Consequently, in figure 5(*c*), the inviscid interaction generates a simple reflection from the cylinder surface post-impingement, while the viscous interaction reveals a reattachment shock formed due to attachment to the separated BL in the interaction zone. Further downstream, at $x = 8$ (figure 5*d*), a Mach stem forms between the incident shock and the cylinder's leeward side, resulting in a lambda-shaped shock structure. A similar feature is also observed between the reflected and incident shocks, thus creating a double-lambda shock system. This double-lambda system persists further downstream, as illustrated in figure 5(*e*). In contrast, the viscous interaction shows a reflected shock detached from the incident shock. This reflected shock is anchored over the primary vortex, as seen in figure 5(*d*), and eventually detaches and moves away from the primary vortex, as seen in figure 5(*e*). The low-speed wake region on the leeward side in the viscous simulations does not sustain the reflected shock.

The 3-D vortical features of the viscous interaction at $Re_D \sim 35\,800$ can be discerned in figure 6. The data are mirrored about the symmetry plane for ease of interpretation and visualisation. A Q-criterion isosurface ($Q = 1$) is used to highlight vortical structures in the mean flow, while inviscid flow features are shown via contours of $|\nabla\rho|$.

An oblique shock is formed at the leading edge of the cylinder, downstream of which a laminar BL develops. The incident oblique shock impinges on this BL at $x \sim 7$, and the resulting adverse pressure gradient leads to the thickening and subsequent separation of the laminar BL from the surface, which reattaches post-interaction. The mean separation and reattachment locations on the windward plane result in a recirculation region on the symmetry plane, spanning $5.92 \leqslant x \leqslant 7.24$. This region is demarcated by isocontours of $u = 0$ in figure 6(*a*). Downstream of the impingement, as the BL reattaches to the surface, the streamline curvature results in an expansion fan. Near the reattachment point,

https://doi.org/10.1017/jfm.2026.12248 Published online by Cambridge University Press

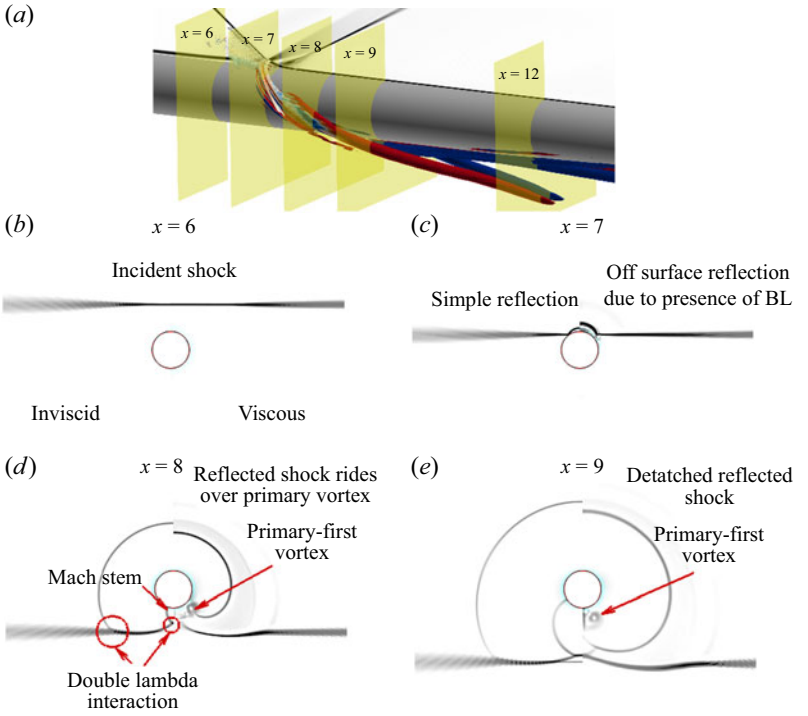


Figure 5. (*a*) Schematic showing the location of various streamwise planes used to represent flow features. Evolution of key viscous and inviscid flow features at four streamwise planes: (*b*) $x = 6$, (*c*) $x = 7$, (*d*) $x = 8$ and (*e*) $x = 9$. The left/right half in each panel shows inviscid/viscous simulation of the interaction. The shock structure is shown via 11 contours of $|\nabla p|$ spaced equally between 0 and 5.

the streamlines align with the downstream direction, resulting in the formation of multiple compression waves that merge to form a reattachment shock.

The mean separation region is highly three-dimensional due to the curvature of the cylinder, introducing a relief effect and allowing the flow to convect azimuthally. As a result, the separation region on the windward plane is smaller compared with an analogous interaction on a flat surface (verified with additional simulations), and it wraps around the cylinder, forming multiple vortices. From the mean flow field, at least three pairs of major vortices are discernible in figure 6. For consistency, we will adopt the following terminology, 'X–Y vortex', while referring to dominant vortical features. Here, 'X' refers to the order of separation, while 'Y' represents the chronological order in which a vortex detaches from the feeding shear layer. This notation is particularly useful in identifying flow topology relevant to slender body aerodynamics, where the separated vortex system forms multiple streamwise-elongated vortex elements (Kumar *et al.* 2020). For example, if present, a primary-first and primary-second vortices will have an identical sense of rotation, as they are generated from the same shear layer (on a given side of the symmetry plane). The primary-first vortex will roll up and separate first from the feeding primary shear layer, while the primary-second vortex will separate subsequently. A primary-first and secondary-first vortices will, however, have an opposite sense of rotation, as they are generated from different shear layers, but both separate first from their respective shear layers (thus have the same chronological order of separation).

https://doi.org/10.1017/jfm.2026.12248 Published online by Cambridge University Press

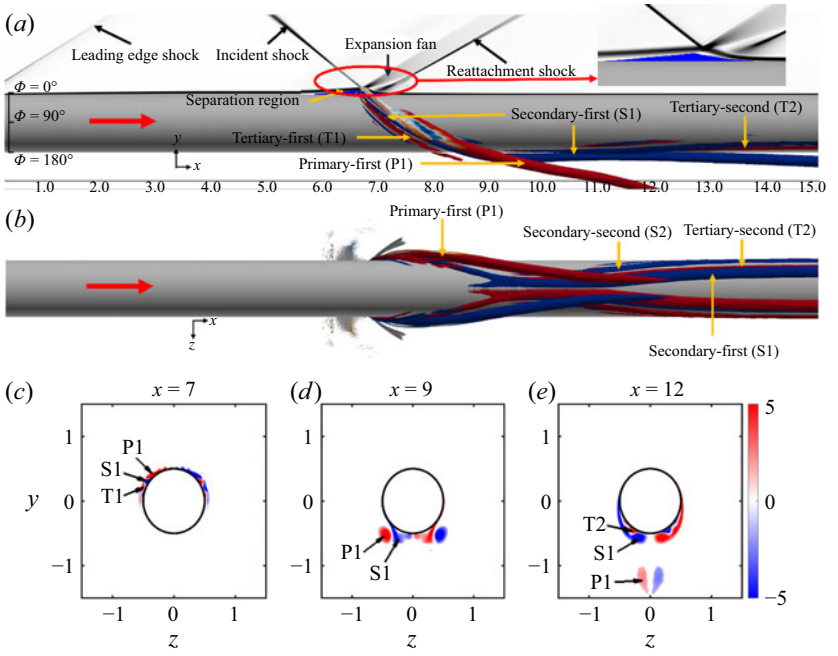


Figure 6. (*a, b*) Mean flow vortical structures are shown via an iso-surface of unity Q-criterion, coloured by streamwise vorticity (ω_x). Inviscid flow features are shown via 101 equally spaced contours of $|\nabla\rho|$ between 0 and 5. The separation region on the windward plane is shown via isocontours of $u = 0$. Red arrows mark the direction of the flow. (*a*) Side view. (*b*) Bottom view. (*c*)–(*e*) Contours of mean streamwise vorticity (ω_x) at the indicated streamwise planes, tracing the generation and evolution of vortical structures. The location of these streamwise planes is shown in figure 5(*a*).

The primary-first vortex originates at the shock impingement location ($x \sim 7$) and detaches from the surface at $\phi \sim 90°$, moving towards the leeward plane and away from the body, as seen in figure 6. Its streamwise variation is better visualised in figure 6(*c–e*), which presents contours of mean streamwise vorticity, ω_x, at three streamwise planes within the region, $7 \leqslant x \leqslant 12$. In figure 6(*c*), as the primary separation wraps around the azimuth, a dominant primary core vortex is visible, which is termed the primary-first (P1) vortex. Beneath it, the secondary-first (S1) vortex core and the tertiary-first (T1) vortex core are visible, with alternating signs on streamwise vorticity. Here, T1 dissipates rapidly as it wraps around the cylinder toward the leeward plane. The corresponding mirrored flow field is also included to aid visual interpretation. Further downstream, at $x = 9$ (figure 6*d*), the P1 vortex core evolves into an elliptic form and detaches from the surface, while S1 remains attached or near the surface and is pushed into the wake. At subsequent streamwise locations (e.g. figure 6*e*), the vortices of the attenuating primary vortex pair move toward each other near the leeward side, while also drifting significantly away from the cylinder.

As seen in figure 6, beyond $x = 9$, the secondary vortex becomes more relevant to near-body flow topology. This vortex pair exhibits a meandering motion where the two vortices come into proximity within the region, $10 \leqslant x \leqslant 11$, before diverging laterally. The full extent of this motion is clearly evident in figure 6(*b*). The region of closest approach is referred to as the 'neck' region of the vortex pair. This behaviour shows qualitative similarities to the long-wavelength instabilities (Crow 1970; Leweke *et al.* 2016) observed in vortex pairs. In addition to their lateral divergence, the vortex pair also lifts away

https://doi.org/10.1017/jfm.2026.12248 Published online by Cambridge University Press

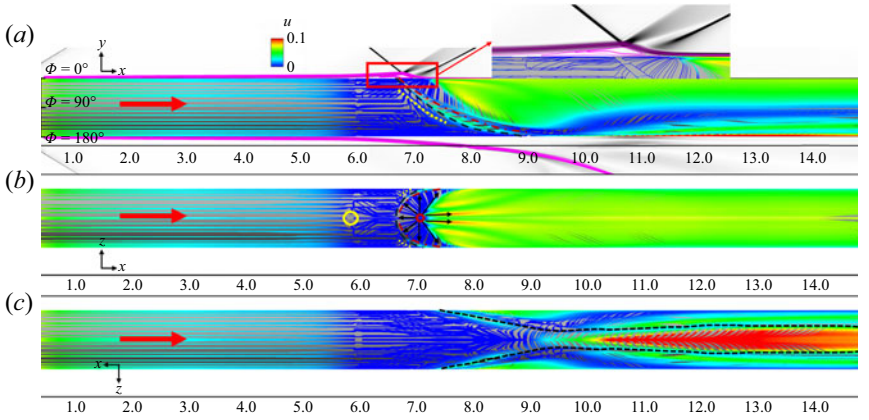


Figure 7. Surface streamlines coloured by streamwise velocity. The maroon lines trace the streamlines on the windward and leeward planes. The red dashed dot line (-.) traces the primary separation, the black dashed line (–) traces the secondary separation and the yellow dotted (:) line traces the first tertiary separation. The red circle, followed by black arrows, marks the location of a source node. Red arrows mark the direction of the flow. (*a*) Side view. (*b*) Top view. (*c*) Bottom view.

from the surface, inducing the formation of a tertiary-second (T2) vortex. The T2 vortex emerges near the neck region of the secondary vortex pair at $x \sim 10$, and grows (figure 6*e*) as the secondary vortex pair moves away from the surface. Additionally, a secondary-second vortex (S2) is observed to be induced by P1, which originates at $x \sim 8$. S2 can be traced in figure 6(*b*), having the same sense of rotation as S1 and evolving adjacent to T2 away from the leeward plane.

The imprint of these flow features is also evident on the surface of the cylinder, as visualised via surface streamlines in figure 7. The streamlines are coloured by streamwise velocity (u) to highlight regions of flow reversal. The maroon lines trace the streamlines of the windward and leeward planes in figure 7(*a*). The separating streamline on the windward plane lifts away from the surface, follows the outer edge of the separation bubble and reverses direction near the reattachment point, moving upstream within the recirculation zone, eventually spiralling into itself to form a stable focus (Perry & Chong 1987) as seen in the inset panel of figure 7(*a*). The primary-first (P1) vortex is observed to emerge from this critical point in the separated flow. A streamline originating just upstream of the mean separation point ($x \sim 5.92$) reattaches near the mean reattachment point ($x \sim 7.24$). This forms a saddle and source node at the separation and reattachment points, respectively, as marked by a yellow and red circle, respectively, in figure 7(*b*). The black arrows indicate the outward omnidirectional behaviour of the streamlines from the source node, consistent with oil flow visualisations by Mason *et al.* (2021). The overall configuration, including saddle, focus and node points, along with the emergence of a horseshoe-shaped pair of counter-rotating vortices, corresponds to the type-1 open 3-D separation topology described by Tobak & Peake (1981). These flow patterns are also comparable with those observed in the laminar SWBLI on a cylinder at Mach 4 by Hung (1983). The surface imprint of the primary separation region is marked by the red dash-dot line, located axially downstream of the other two separation regions. The spatial imprint of this region on the surface vanishes in the leeward half of the geometry due to the primary vortex pair drifting away from the cylinder surface.

The imprint of the secondary separation is most prominent on the surface, since the associated vortex pair remains close to the wall and is marked by a black dashed line

https://doi.org/10.1017/jfm.2026.12248 Published online by Cambridge University Press

in figure 7. As seen earlier, this separation begins beneath the primary separation on the windward plane but eventually moves upstream of the primary separation as the vortex wraps around the cylinder on the leeward side. The meandering behaviour is clearly visible on the leeward side of the body, particularly around the neck region at $x \sim 10$ in figure 7(c). The tertiary separation region induced by the T1 vortex, marked by the yellow dotted line, is upstream of the secondary separation and disappears rapidly. On the leeward plane, the separating streamlines never reattach, with the region beneath being occupied by secondary vortices approaching circumferentially.

The outer inviscid flow and the vortex system generated during the interaction result in strong cross-flow patterns over the cylinder. Downstream of the interaction region, a strong cross-flow is generated over the cylinder surface, primarily due to the change in post-shock free-stream conditions, which effectively induces a negative angle of attack. The increased pressure on the windward side drives the flow tangentially away from the windward plane and towards the leeward plane, thus thickening the leeward BL. However, on the leeward side, streamlines diverge away from the leeward plane with negative cross-flow velocity towards the S1 vortex pair due to the pressure gradient between the high-pressure wake and the low-pressure vortex system. The azimuthal variation of the separation region size, delineated by upstream-travelling streamlines and bounded by the mean separation and reattachment streamlines, exhibits quasi-conical similarity (Settles & Teng 1984) in this interaction.

Analogous to similarities between 2-D-SWBLIs and compression corner flows, the surface topology identified in the present axi-SWBLI case has similarities with that observed in cylinder-offset flare interactions, for example, as reported in Gaitonde *et al.* (1997) and Gaitonde (2015). In particular, the separation-induced primary vortex system, open separation regions over curved surfaces and the formation of a stable focus from which horseshoe-shaped vortical structures originate, are consistent features across these scenarios.

5. Aerodynamic loading

Axi-SWBLIs can induce large pressure gradients and harbour localised regions of high mean shear over the surface. This is evaluated using the mean pressure coefficient and skin friction coefficient on the surface of the cylinder in figures 8(a) and 8(b), respectively. While the former represents normal forces experienced by the surface, the latter is associated with shear loading. The wall pressure coefficient, C_p, is calculated as

$$C_p = \frac{p^* - p^*_\infty}{\frac{1}{2}\rho^*_\infty u^{*2}_\infty} = 2(p - p_\infty) \tag{5.1}$$

.

Skin friction coefficient, C_f, is calculated as

$$C_f = \frac{\tau^*_w}{\frac{1}{2}\rho^*_\infty u^{*2}_\infty} = \frac{\mu^*_w}{\frac{1}{2}\rho^*_\infty u^{*2}_\infty}\frac{\partial u^*}{\partial y^*_n}\bigg|_{y^*_n=0} = \frac{2}{\mathrm{Re}}\mu_w \frac{\partial u}{\partial y_n}\bigg|_{y_n=0}, \tag{5.2}$$

where, y_n is the wall-normal coordinate.

The imprint of the impinging shock over the surface diminishes from the windward to leeward side, resulting in a wall pressure distribution as shown (by C_p) in figure 8(a).

https://doi.org/10.1017/jfm.2026.12248 Published online by Cambridge University Press

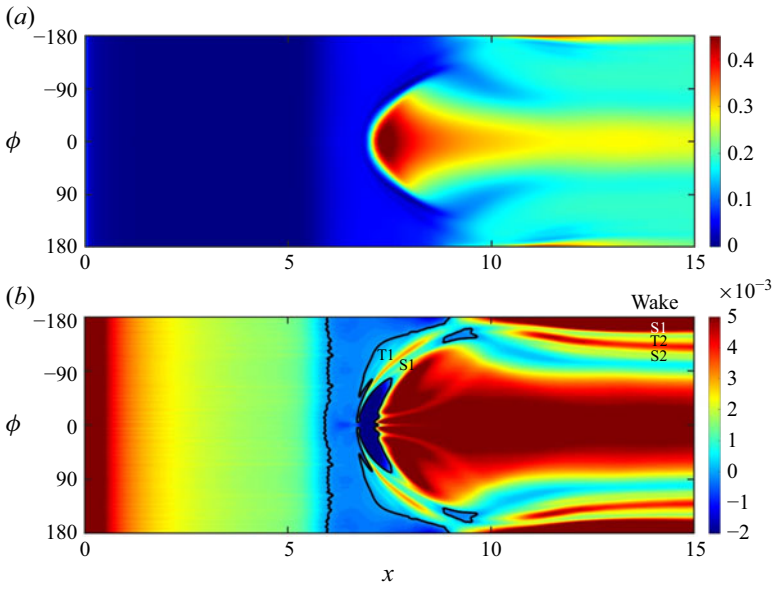


Figure 8. Variation of (*a*) pressure coefficient (C_p) and (*b*) skin friction coefficient (C_f) on the surface of the cylinder. The solid black line represents iso-contours of $C_f = 0$.

However, the separation induced by the strong adverse pressure gradient results in low-velocity regions that have higher pressure in comparison with the ambient. The steep rise in pressure observed on the windward plane is due to the reattachment shock. Across the azimuthal planes moving away from the windward plane, the pressure rise follows the conical shape of the reattachment shock, seen earlier in figure 2. Close to the leeward plane, regions of increased pressure are evident, particularly post $x \sim 10$, which correspond to the downstream of the neck region, where the meandering secondary-first (S1) vortex pair diverges (see figure 6*b*). These features are in line with those observed in experiments by Mason *et al.* (2021) and Wahidi *et al.* (2024).

The skin friction coefficient is shown in figure 8(*b*). The blue regions demarcated by the solid contour lines represent areas of negative streamwise velocity, signifying flow reversal and separation. On the windward plane, as the BL reattaches and begins to grow, the fuller nature of the velocity profiles leads to an increase in wall shear loading. The smallest separated flow region is observed on the windward plane, while the largest is located on the leeward plane, with the separation line displaying a quasi-2-D separation line. This occurs because the cross-flow induced by the shock convects the flow away from the windward plane toward the leeward plane, leading to a thicker BL on the leeward side (Hung 1983), and hence stronger upstream influence. The secondary-first and tertiary-first vortex pairs, being relatively closer to the wall, have the strongest impact on shear loading. Regions between these two counter-rotating vortices show an elevated skin friction due to the downwash of the fluid towards the wall (Hader & Fasel 2019). The imprint of the secondary separation (S1), as it evolves from the windward to the leeward plane, is thus approximately traced by the inner edge of the elevated C_f streak between $6.5 \leqslant x \leqslant 9.5$ in the wake region. As this vortex pair develops and meanders on the leeward side, a significant increase in skin friction coefficient is observed in regions between the two vortices and the wake. This could be attributed to increased turbulent activity in the wake (discussed in the subsequent section) as well as the breakdown of the S1 vortex.

https://doi.org/10.1017/jfm.2026.12248 Published online by Cambridge University Press

Additionally, the counter-rotating tertiary-second (T2) and secondary-second (S2) vortices induce strong positive shear stress in the region between them. These trends highlight significant spatial variations in wall loading caused by axi-SWBLIs.

6. Unsteady characteristics of the interaction

6.1. *Fluctuation statistics*

Although the incoming BL is laminar, the SWBLI induces strong fluctuations that can transition the BL and lead to breakdown of the vortical structures, resulting in strong amplification of turbulence intensity and unsteadiness. To quantify this and to gain insights into the mechanisms driving this amplification, a budget analysis of the turbulent kinetic energy (TKE) is presented in this section, which identifies regions where fluctuation energy is concentrated and phenomena resulting in its redistribution. When applied to such transitional flows, the TKE analysis identifies regions within the flow that are most sensitive to perturbation amplification and physical mechanisms in the base flow that eventually promote the generation and distribution of turbulence. Further, all terms in the transport equation for TKE (applicable to a generic flow field exhibiting statistical stationarity) can be explicitly calculated from the computed data. The transport equation for $TKE(k) = (1/2)\widetilde{u_i'' u_i''}$ is symbolically represented as

$$\frac{\partial \bar{\rho} k}{\partial t} = C + T + P + V - \bar{\rho}\varepsilon + K, \tag{6.1}$$

including the terms, convection (C), turbulent transport (T), production (P), viscous diffusion (V), dissipation ($\bar{\rho}\varepsilon$) and compressibility effects (K). In the above, quantities with a bar ($\overline{q}$) represent Reynolds-averaged terms, while quantities with a tilde ($\widetilde{q}$) denote Favre-averaged terms. Fluctuating components of a quantity, q, are defined as $q' = q - \overline{q}$ for Reynolds decomposition and $q'' = q - \widetilde{q}$ for Favre decomposition. Convergence of statistical quantities is ensured by evaluating the statistics using data segments of varying temporal durations. Three key azimuthal planes, $\phi = 0^o$, 90^o and $\phi = 180^o$, will be utilised for analysing the TKE properties. Key inferences are drawn by summarising the properties of TKE, its production ($P = -\bar{\rho}\widetilde{u_i'' u_j''}(\partial \tilde{u}_i/\partial x_j)$) and transport mechanisms such as convection terms ($C = -(\partial \bar{\rho} \tilde{u}_j k/\partial x_j)$) and turbulent transport ($T = -(\partial/\partial x_j)[(1/2)\bar{\rho}\widetilde{u_i'' u_i'' u_j''} + \overline{p' u_j''}]$), in figure 9.

Figures 9(*a*), 9(*b*) and 9(*c*) show TKE, production and convection contours, respectively, near the interaction zone on the $\phi = 0^o$ windward plane. Line contours of density gradient magnitude ($|\nabla\rho|$) from the mean flow field are included for contextual clarity. It has to be noted that the BL on this plane does not undergo complete transition to turbulence, and the TKE budget on this plane primarily identifies fluctuating energy due to coherent motions and instability amplification within the separation region. Peak TKE levels are observed within the downstream half of the recirculation region and in the reattaching BL. These regions of elevated TKE also correspond to regions with strong TKE production, as seen in figure 9(*b*). The primary mechanism driving TKE production in the separation zone upstream of shock impingement are the strong streamwise velocity fluctuations ($\widetilde{u''u''}$), in conjunction with large negative streamwise gradients of streamwise velocity ($\partial \tilde{u}/\partial x$), arising from flow deceleration. Downstream of shock impingement, strong vertical gradients of streamwise velocity ($\partial \tilde{u}/\partial y$) in conjunction with Reynolds stresses arising from anti-correlation of streamwise and vertical velocity fluctuations ($\widetilde{u''v''}$) drive production. Here, the components that were active upstream of shock impingement behave

https://doi.org/10.1017/jfm.2026.12248 Published online by Cambridge University Press

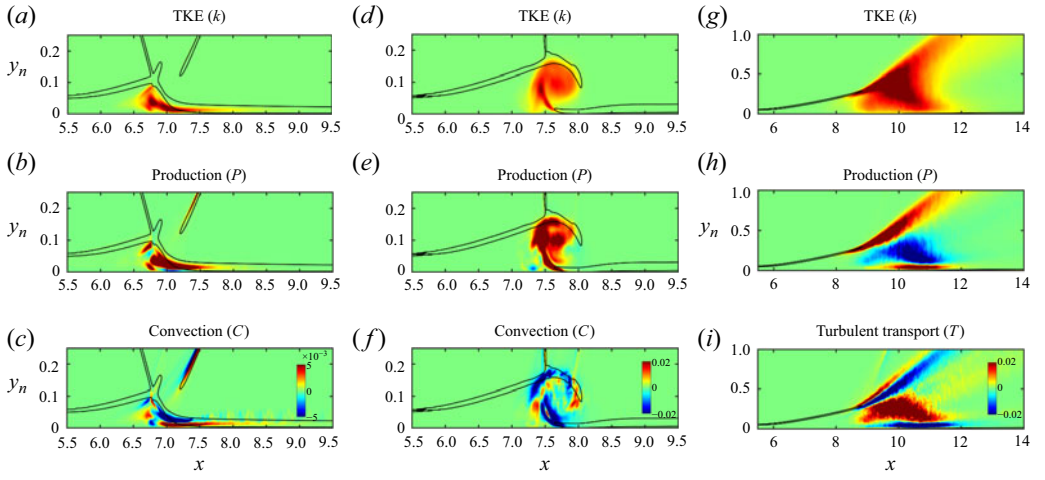


Figure 9. Contour plots of various terms in the TKE transport equation(6.1) on three azimuthal planes. $(a,b,c) - \phi = 0°$, $(d,e,f) - \phi = 90°$, $(g,h,i), - \phi = 180°$. Mean flow (black line) is shown via isocontour lines of $|\nabla \rho|$. Frames in each column have the same contour levels.

as a TKE sink. This behaviour is qualitatively similar to the mechanism of unsteadiness amplification seen in turbulent SWBLI on a flat plate by Fang *et al.* (2020). Transport of TKE away from zones of peak fluctuations mainly happens in the reattaching shear layer and is dominated by mean flow convection, as suggested by the blue zone in figure 9(*c*). Convection further aids in TKE transport post-reattachment within the BL.

A similar TKE budget analysis for the $\phi = 90°$ plane is shown in figures 9(*d*), 9(*e*) and 9(*f*), which plane intersects the region where the separated shear layer rolls up into the primary and secondary vortices. The focus here is on the turbulent breakdown of the vortex rather than the reattached BL, which shows no signs of transition. Peak TKE values are observed in the nascent separating S1 shear layer as it detaches from the surface and at the core of the vortex (figure 9*d*). TKE production peaks in the separating shear layer and the vortex core, indicating that intense velocity gradients in this region are the primary source of turbulence generation. While production in the separating shear layer is driven by azimuthal gradients, that in the rolled-up vortex region is driven by wall-normal gradients. The streamwise velocity gradients were observed to show sink-like behaviour in the region of the vortex periphery. Regions of peak TKE redistribution align with those of peak TKE production, and convection is the primary mechanism of transport away from regions of peak TKE in the vortex periphery and the detaching shear layer (Schanderl *et al.* 2017). This is driven by strong mean flow gradients, as is evident from the location of the mean flow isocontour lines.

The TKE budget on the leeward plane ($\phi = 180°$) is reported in figures 9(*g*), 9(*h*) and 9(*i*), which plane includes the wake region. Peak TKE levels are present in the spreading shear layer and the wake. It should be noted that peak TKE values observed on this plane are significantly higher than those seen on the other azimuthal planes, indicating a monotonic increase in intensity of fluctuations from the windward to the leeward plane. The TKE production is dominant in the outer shear layer driven by strong streamwise velocity correlations ($\widetilde{u''u''}$) and strong streamwise and wall-normal gradients. In addition, a sink-like behaviour is observed towards the inner regions of the shear layer near reattachment, driven by strong anti-correlation between streamwise and wall-normal

https://doi.org/10.1017/jfm.2026.12248 Published online by Cambridge University Press

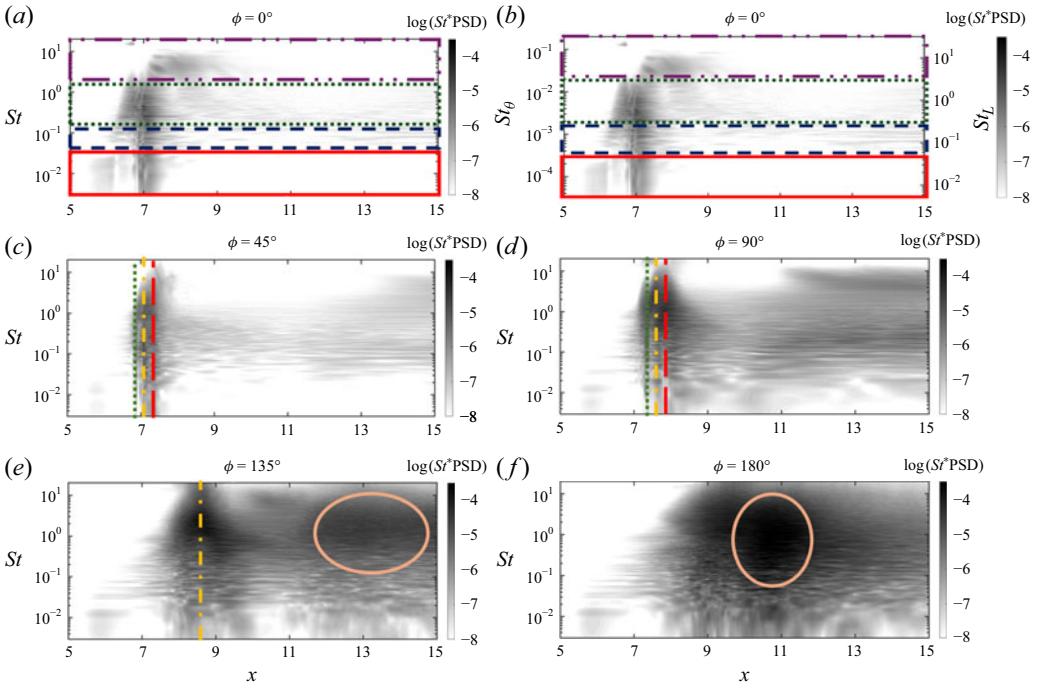


Figure 10. Streamwise variation of pre-multiplied wall pressure spectra at select azimuthal angles around the cylinder. The rectangles in panels (*a* and *b*) demarcate the very-low-, low-, mid- and high-frequency dynamics. The red dashed line, the yellow dash-dot line and the green dotted line mark the signatures of primary, secondary and tertiary separations. The orange ovals in (*e* and *f*) demarcate zones of interest. Here, PSD is the power spectral density.

velocity fluctuations ($\widetilde{u''v''}$) and strong wall-normal velocity gradients ($\partial\tilde{u}_i/\partial y$). This suggests that high TKE levels observed in this region are not directly produced here, but rather transported to these regions. This is evidenced by strong negative regions of turbulent transport in the outer shear-layer zones (indicating transport away from this region) and strong positive regions in the inner shear layer (indicating transport towards this region). It has to be noted that on the leeward plane, turbulent transport is dominant over the convection term.

While the turbulent characteristics of the windward plane of the axi-SWBLI showed similarities with a 2-D-SWBLI, those characteristics significantly varied across the azimuthal planes. This highlights the strong azimuthal dependence of turbulence intensity within the interaction and the mechanisms responsible for the production and distribution of TKE.

6.2. *Interaction spectra*

The previous section revealed the spatial inhomogeneity of unsteadiness in the axi-SWBLI. To quantify the temporal dynamics associated with it, here, we analyse the wall pressure fluctuations using the pre-multiplied spectra at 5 equally spaced azimuthal planes around the cylinder. The streamwise evolution of these spectra at five representative azimuthal planes ($\phi = 0°$, 45°, 90°, 135°, 180°) is presented in figure 10.

Being a plane of symmetry, the windward plane exhibited characteristics of 2-D-SWBLI in the mean flow field and TKE characteristics. We now evaluate whether this similarity

https://doi.org/10.1017/jfm.2026.12248 Published online by Cambridge University Press

is exhibited in its temporal dynamics as well. Previous literature (Dussauge *et al.* 2006; Pirozzoli & Grasso 2006; Piponniau *et al.* 2009; Clemens & Narayanaswamy 2014) has identified that the dynamics of the separation region in 2-D-SWBLIs scales with the length of the separation bubble. Therefore, the spectrum on the windward plane ($\phi = 0°$) in figure 10(*a*) is re-plotted with appropriately scaled axes in figure 10(*b*). The right-side axis in figure 10(*b*) represents the Strouhal number based on the length of the separation region ($L^* \sim 1.32D^*$) on the windward plane as the reference length, defined as, $St_L = (f^*L^*/u^*)$. In addition, the instabilities associated with the BL and the separated shear layer are often observed to scale with the momentum thickness of the BL prior to separation (Michalke 1965; Hussain 1986; Lakshmi Narasimha Prasad & Unnikrishnan 2024). Therefore, the left-hand side axis in figure 10(*b*) shows the Strouhal number based on the momentum thickness (θ^*) of the BL prior to flow separation on the windward plane as the reference length, defined as, $St_\theta = (f^*\theta^*/u^*)$. This scaling facilitates interpretation of the spectral content by relating distinct frequency bands to characteristic length scales associated with the global separation dynamics and local shear-layer instabilities in the context of existing literature.

The spectra on the windward plane in figures 10(*a*) and 10(*b*) show reasonable agreement with distinct bands of unsteadiness that have been reported in turbulent 2-D-SWBLI Adler & Gaitonde (2018). It has to be noted that the studies by Adler & Gaitonde (2018) and Gaitonde & Adler (2023) were primarily on turbulent SWBLIs and therefore, the inferences from these works are primarily invoked here to contextualise the observed spectral organisation in the current interaction. A very-low-frequency band is evident at frequencies, $St/St_L \leqslant 0.03/0.04$, marked by the solid red rectangle, which initiates near the separation point and achieves maximum amplification within the interaction region. This is reminiscent of the low-frequency 'bubble breathing' motion seen in 2-D-SWBLI (Délery & Dussauge 2009; Clemens & Narayanaswamy 2014). As shown by Piponniau *et al.* (2009), the streamwise movements of the bubble are associated with its contractions and dilations. This variation in bubble size results from the transfer of mass, momentum and vorticity between the recirculating region and the external flow. Additionally, it was shown that the entrainment induced by the mixing layer plays a significant role in this process.

A low-frequency band centred around $St/St_L \sim 0.08/0.1$ is marked by the blue dashed rectangle. This band is predominantly seen near reattachment ($x \sim 7.5$), and is associated with the oscillation of the reattaching shear layer. Gaitonde & Adler (2023) associate this band with secondary oscillations of the separation bubble. A recent study by Malmir *et al.* (2024) observed this low-frequency unsteadiness in a pressure-induced laminar separation bubble, which they attributed to the 'flapping' of the reattaching shear layer, characterised by a low-frequency wavering motion of the shear layer. Thus, the two frequency bands at the lower end of the spectra represent the 'breathing' and 'flapping' motions of the separation zone. As noted in Malmir *et al.* (2024), during bubble breathing, both the separation and reattachment points exhibit upstream and downstream motion and are characterised by a growth and collapse in the size and length of the separation bubble. In contrast, the flapping is characterised by a low-frequency motion of the reattachment point in the streamwise direction.

The mid-frequency band originating post-separation and extending all the way until reattachment, in the range of $0.1/0.13 \leqslant St/St_L \leqslant 1.5/2$ (marked by the green dotted rectangle), corresponds to shedding from the shear layer and flapping of the reattachment shock. When scaled with the momentum thickness of the BL, this band falls within $0.0012 \leqslant St_\theta \leqslant 0.018$. Several previous studies (Michalke 1965; Ho & Huerre 1984; Hussain 1986; Bogey 2022; Lakshmi Narasimha Prasad *et al.* 2025*a*) have demonstrated

https://doi.org/10.1017/jfm.2026.12248 Published online by Cambridge University Press

that the predominant instability in a shear layer, the Kelvin–Helmholtz (K-H) instability, lies in the range of $0.005 \leqslant St_\theta \leqslant 0.032$. This further confirms that the frequencies observed in this mid-frequency band can be attributed to the shedding of coherent vortices from the shear layer, driven by the K-H instability.

The spectra also contain a high-frequency band above $St/St_L \sim 2/2.5$, marked by the purple dashed double dotted rectangle. Gaitonde & Adler (2023) observed convection of 'integral-scale turbulent fluctuations' in this spectral range, which entered through the incoming BL in turbulent interactions, with peak energy upstream of the separation point. However, given the laminar nature of the upstream BL in the current case, this band appears predominantly downstream of the separation point, where the shear layer undergoes breakdown and reattaches into a BL. Therefore, this high-frequency band can be attributed to the convection of coherent structures in the BL post-reattachment. The rapid decay of the high-frequency content in the reattached BL, along with the lower root-mean-square levels of velocity fluctuations observed post-reattachment in figure 9(*a*), suggests that the BL does not transition post-reattachment.

The qualitative nature of the spectra varies rapidly across the azimuth, owing to the open separation and 3-D nature of the vortex system and wake. At $\phi = 45°$, three distinct broadband signatures are identifiable, as marked in figure 10(*c*). The red dashed line traces the primary separation, while the yellow dash-dot line traces the secondary separation. Faint traces of the tertiary separation are marked by the green dotted line. As noted earlier, while discussing the mean flow structures, the wall signature of primary separation appears downstream of the secondary and tertiary separations. At $\phi = 90°$, in figure 10(*d*), all three separation regions exhibit characteristics of breakdown to turbulence, evident from the increased energy at higher St values. This azimuthal location also marks the location where the primary vortex moves away from the surface, reducing its wall imprint on subsequent azimuthal planes. The lack of significant spectral content and energetic amplification of the high-frequency band downstream of $x \sim 9$ in the range $0° \leqslant \phi < 90°$ indicates the primarily laminar state of the BL. At $\phi = 135°$ in figure 10(*e*), the breakdown of the secondary vortex pair is dominant, characterised by a broadband energetic peak centred around $St \sim 2$. Further downstream, between $12 \leqslant x \leqslant 14$, broadband energy peaks appear in the frequency range, $1 \leqslant St \leqslant 10$, as highlighted by the orange curve. This corresponds to the breakdown of the tertiary-second (T2) vortex pair. On the leeward plane ($\phi = 180°$), a highly turbulent wake is observed. Notably, the peak amplitudes of fluctuations are observed as a broadband energetic peak between $10 \leqslant x \leqslant 12$, with energy levels surpassing those on all the other planes. This location aligns with the region where the meandering secondary vortex pairs converge to form the neck region.

An interesting observation here is that, despite the qualitative changes in the dynamics across the azimuthal planes, the separation point ($x = 5.92$) remains relatively fixed around the cylinder. This spatial location exhibits the very-low-frequency motion of the separated flow, centred around $St \sim 0.01$, as observed on all azimuthal planes. This suggests that the very-low-frequency dynamics of the separation point may be independent of the three-dimensionality induced by the surface curvature of the axisymmetric body. This observation is particularly interesting in light of the findings of Gaitonde & Adler (2023), who report a suppression of the low-frequency separation-point dynamics in conical swept SWBLI configurations. In contrast, the present low-Re_D interaction, while exhibiting quasi-conical symmetry in the mean separation and reattachment streamlines (figure 7), retains strong low-frequency unsteadiness. This coexistence of quasi-conical flow organisation and the pronounced low-frequency dynamics in axi-SWBLIs highlights its key distinction from swept SWBLIs over flat surfaces.

https://doi.org/10.1017/jfm.2026.12248 Published online by Cambridge University Press

Number of snapshots	Sampling frequency (St)	Window	Overlap	Number of blocks (n_{blk})	Number of frequencies (n_{fft})
26 800	40	10 000	50 %	4	10 000

Table 1. Parameters used for SPOD.

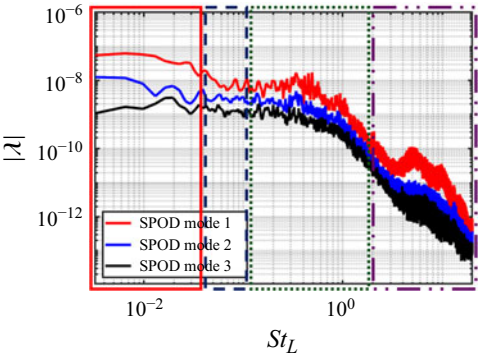


Figure 11. Eigenvalue spectra obtained from SPOD. The zones marked in this plot are identical to those in figure 10.

6.3. *Spatio-temporal support of interaction spectra*

Similarity with 2-D-SWBLI was invoked above to identify the physical significance of various components within the axi-SWBLI interaction spectra. We now obtain the spatial support of key spectral bands using spectral proper orthogonal decomposition (SPOD) (Towne *et al.* 2018; Schmidt & Colonius 2020), to provide insights into the flow structures associated with the observed unsteadiness. Consistent with the spectral analysis, the results are first presented on the windward plane. The SPOD is performed separately on both pressure and streamwise velocity fluctuation data on the windward plane, focusing on a subdomain that is most dynamically active. This region spans $5 \leqslant x \leqslant 10$ and $0 \leqslant y_n \leqslant 0.2$, where, y_n represents the wall-normal distance. Parameters used to perform SPOD are listed in table 1.

Figure 11 presents the eigenvalue spectra obtained from SPOD. The various bands of frequencies observed in the pressure spectra (shown previously in figure 10) are also marked here. The very-low-frequency band is marked by the red solid rectangle, where a significant band gap between the first and subsequent modes indicates low-rank behaviour. Two peaks ($St_L \sim 0.08$ and 0.1) are visible in the zone marked by the blue dashed rectangle, corresponding to a low-frequency dynamics. The green dotted rectangle marks the mid-frequency band, featuring multiple peaks centred around $St_L \sim 0.4$. The purple dash double dot rectangle demarcates the zone of high frequency, where a broad peak centred around $St_L \sim 4.5$ is observed with a significant rank gap with the sub-dominant modes. Across all frequencies, SPOD mode 1 is observed to capture more than 55 % of the total energy at any given frequency, indicating the low rank nature of the dynamics on the windward plane.

Representative real parts of the dominant SPOD eigenmodes (SPOD mode 1) within each frequency band identified in figure 11 are displayed in figure 12, as evaluated from streamwise velocity fluctuations. The background image shows contours of $|\nabla\rho|$,

https://doi.org/10.1017/jfm.2026.12248 Published online by Cambridge University Press

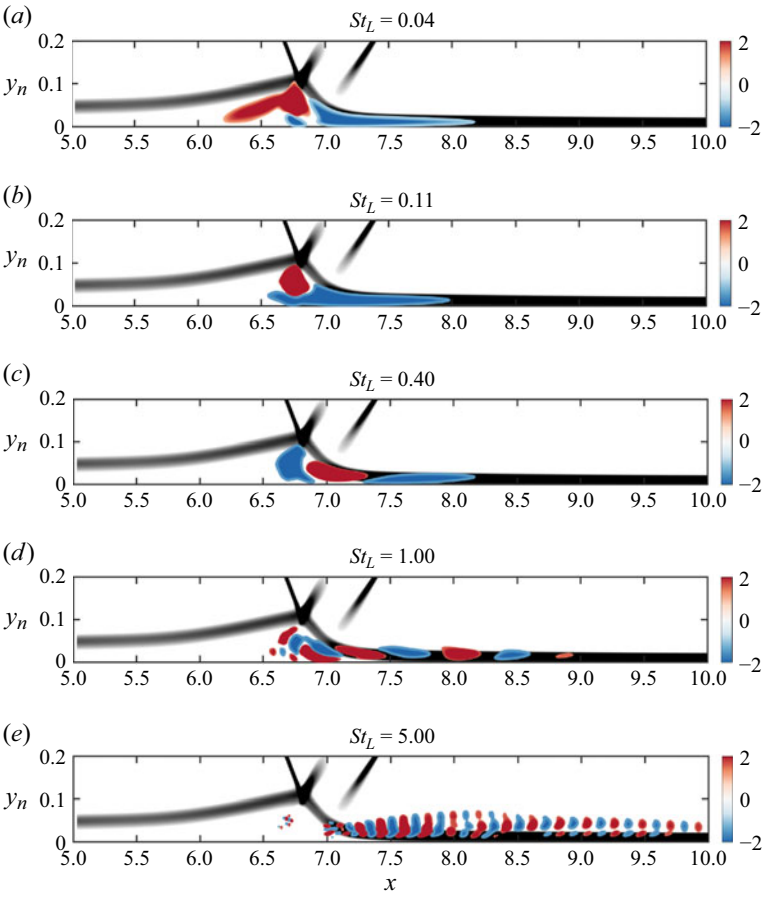


Figure 12. Real part of SPOD eigenmodes at four representative frequencies within the bands highlighted in figure 11. The background image shows contours of $|\nabla\rho|$ that highlight the mean flow features observed on this plane. The foreground image shows isocontour lines of the dominant SPOD eigenmode at each frequency.

highlighting the mean flow features on this plane. The foreground image presents contours of the dominant SPOD eigenmode at the specified frequencies. In the very-low-frequency regime, the mode at $St_L \sim 0.04$ (figure 12*a*) has predominant spatial support in the separation bubble, indicating large-scale oscillations associated with the separated flow. In addition, this mode shows a phase shift from the separation point to the reattachment point, resulting from opposing tendencies of motion associated with these oscillations. This behaviour is typical of the 'breathing' motion of separation bubbles (Nichols *et al.* 2017; Khobragade *et al.* 2022), resulting from growth and dilation. The modal structure at this frequency also aligns very well with that observed in low-frequency response modes obtained from resolvent analysis for a laminar SWLBI at a low spanwise wavenumber (β) by Bugeat *et al.* (2022), and shows similarities to the stationary global mode seen in studies by Robinet (2007). Since the BL prior to shock impingement is laminar, upstream forcing of the separation region is minimal. Therefore, the primary mechanism driving this very low frequency can be attributed to the presence of global instabilities harboured by the separation region (Robinet 2007; Touber & Sandham 2009; Nichols *et al.* 2017). Rodriguez & Theofilis (2010), using bi-global stability analysis, showed that such global instabilities can be self-excited for a finite range of wavenumbers when reverse flow

https://doi.org/10.1017/jfm.2026.12248 Published online by Cambridge University Press

exceeds 7 %, which is satisfied in the current case. While studies by Sansica *et al.* (2016) and Bugeat *et al.* (2022) emphasise the necessity of external forcing and highlight the lack of a self-sustaining mechanism for the low-frequency unsteadiness, they also suggest that upstream-travelling waves originating from instability mechanisms or laminar–turbulent transition in the downstream portion of the interaction region could act as a source of such forcing.

Figure 12(*b*) shows the mode at $St_L \sim 0.1$, which belongs to the low-frequency regime. This mode is predominantly sustained in the region of peak reversed flow and the reattachment zone. This aligns well with the flapping motion of the shear layer discussed in Agostini *et al.* (2012) and Malmir *et al.* (2024), accompanied by 'wavering' of the shear layer and vertical displacement of the separation zone. In the mid-frequency regime, at $St_L \sim 0.4$, the mode (figure 12*c*) displays spatial support within and downstream of the reattaching shear layer. This mode highlights coherent convecting structures being generated from the bubble and the shear layer, suggesting that this frequency band is associated with large-scale vortex shedding, in line with the findings of Kiya & Sasaki (1983). Although not included for brevity, the SPOD eigenmodes of pressure fluctuations at this frequency also highlighted the reattachment shock, indicating strong coupling between the shedding of large-scale coherent vortices and the oscillations of the reattachment shock. The mode at $St_L \sim 1$ (figure 12*d*) corresponds to the dominant K-H instability in the shear layer. This mode is characterised by the formation of coherent vortices within the shear layer and subsequent shedding of these vortices near reattachment. This frequency also corresponds to $St_\theta \sim 0.012$, which lies within the band of frequencies where the K-H shedding has been reported in the literature (Simoni *et al.* 2017; Khobragade *et al.* 2022). The spatial support for the high-frequency band, $St_L \sim 5$, shown in figure 12(*e*), corresponds to fine-scale structures in the reattaching shear layer that are subsequently amplified in the BL after reattachment.

The spectral and modal comparisons presented here thus confirm the similarities between the dynamics in 2-D-SWBLIs and axi-SWBLIs near the windward symmetry plane and deviations from it along the azimuthal coordinate. A global modal analysis accounting for 3-D effects will be presented in the next section, following characterisation of the wake dynamics on the leeward side.

7. Vortex dynamics

The presence of prominent vortex pairs induces strong unsteadiness on the leeward side of the cylinder, as seen in figure 10(*e*), which is quantified in detail in this section. The highly 3-D nature of these vortices necessitates comprehensive spatial probing of data to fully understand the non-homogeneous nature of wake unsteadiness. To this end, we first track the unsteadiness developing along the primary and secondary vortex trajectories, beginning at the interaction zone. At any given streamwise location, these vortex trajectories are identified using a vortex-core detection criterion, based on the local maximum/minimum of ω_x for the secondary/primary vortex pair in a suitable subdomain encompassing these vortices at each streamwise plane. As seen earlier in figure 6 and in the inset in figure 13(*a*), the trajectory of the primary vortex core eventually detaches and drifts away from the cylinder, while the secondary vortex core remains in proximity to the surface of the cylinder. Necking is also observed at $x \sim 10$.

Spatial variation of pressure fluctuation spectra extracted along the trajectories of the primary and secondary vortex cores is presented in figures 13(*a*) and 13(*b*), respectively. This highlights unsteadiness harboured by the 3-D vortex system, as it wraps around the azimuth and evolves into a streamwise-aligned orientation. To facilitate comparisons with

https://doi.org/10.1017/jfm.2026.12248 Published online by Cambridge University Press

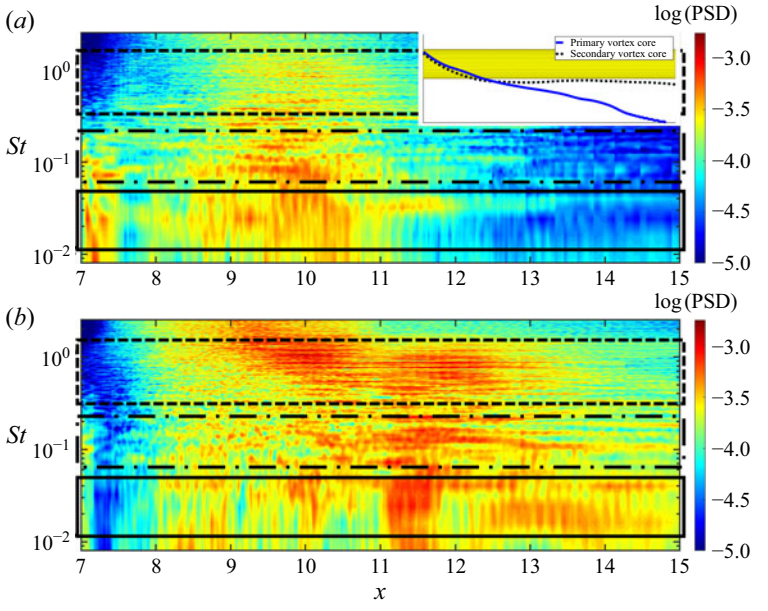


Figure 13. Streamwise variation of the logarithm of PSD of pressure fluctuations obtained along the trajectory of the (*a*) primary and (*b*) secondary vortex cores. The inset figure in (*a*) shows the extracted trajectories of the vortex cores.

flow features seen in § 4 and their dynamics, the abscissa is retained as the streamwise coordinate (x). Comparing the two spectral distributions, it is evident that the energy associated with the dynamics of the secondary vortex pair is stronger than that of the primary vortex. Due to its proximity to the surface, this can significantly affect the unsteady loading experienced by the body.

Both vortices harbour very-low-frequency unsteadiness at $St \sim 0.03-0.04$ (marked by the solid rectangle), which lies in the vicinity of the bubble breathing frequency observed on the windward plane in figure 10. While it appears in the primary vortex system near the interaction, the secondary vortex system sustains it further downstream ($\sim x \geqslant 12$), within the leeward wake. This suggests that the low-frequency unsteadiness of the separated flow induces large-scale oscillations in the vortex pairs as the bubble grows and collapses on the windward plane. In addition, the secondary vortex demonstrates strong energetic bands at $St \sim 0.1-0.2$ (marked by a dash-dotted rectangle). These frequencies lie in the range where meandering (Green & Acosta 1991) of vortices is observed in wakes (Garmann & Visbal 2019; Zigunov *et al.* 2020; Ranjan *et al.* 2022), and are often dominated by the short-wavelength elliptic instability (Kerswell 2002; Shahriar *et al.* 2023) of the associated vortex pairs. These spectral bands are also seen in the primary vortex, but at much lower amplitudes. High-frequency fluctuations (marked by a dashed rectangle) corresponding to vortex breakdown are also observed near $x \sim 10$ in both vortex pairs. These high-frequency components are relatively more intense in the secondary vortex pair due to its proximity to the leeward wake, where peak turbulent mixing exists, as observed in figure 9.

To verify the above hypothesis about elliptic instabilities, we extract the energetic structures in these vortex systems at a fixed streamwise plane encompassing the leeward wake. Although multiple streamwise planes were tested, key observations are summarised using a representative plane at $x = 12$. The dominant vortex instabilities and their associated motion are extracted using the proper orthogonal decomposition (POD)

https://doi.org/10.1017/jfm.2026.12248 Published online by Cambridge University Press

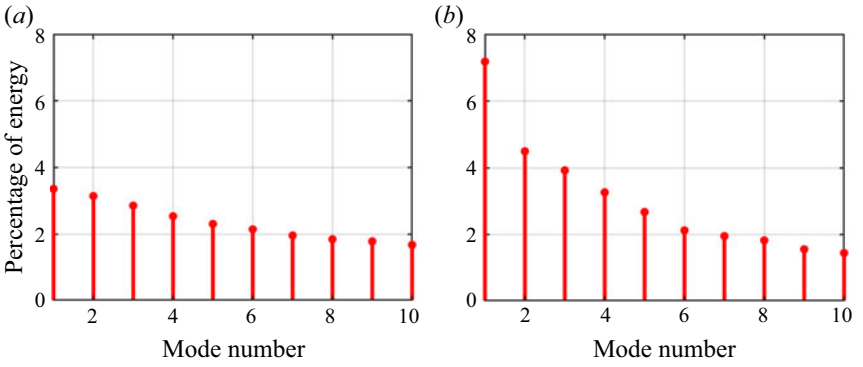


Figure 14. Energy content distribution across POD modes for (*a*) P1 vortex pair and (*b*) S1/T2 vortex pairs at $x = 12$.

(Berkooz *et al.* 1993) applied to the streamwise vorticity field (ω_x'), following prior works (Zigunov *et al.* 2020; Ranjan *et al.* 2020). The POD facilitates a decomposition of variables into energetically optimal spatial modes and temporal coefficients. Thus, a fluctuating field, $\boldsymbol{q}'(\boldsymbol{x}, t)$, can be represented as follows:

$$\boldsymbol{q}'(\boldsymbol{x}, t) = \sum_{n=1}^{\infty} a_n(t)\boldsymbol{\phi}_n(\boldsymbol{x}), \tag{7.1}$$

where $\boldsymbol{x} = [x, y, z]$ is the position vector, $a_n(t)$ are the temporal coefficients and $\boldsymbol{\phi}_n(\boldsymbol{x})$ are the spatial modes. A total of 2500 snapshots sampled at a non-dimensional time of $\Delta t = 0.2$ are utilised for the decomposition, which is performed separately on the isolated P1 and S1/T2 vortex pairs. This is done to prevent the energetic S1/T2 vortex pairs from masking the dynamics of the P1 vortex system.

Figure 14 shows the distribution of energy in the first ten POD modes for the P1 vortex pair (*a*) and the S1/T2 vortex pairs (*b*) at $x = 12$. Due to the turbulent nature of the leeward wake, neither vortex pair exhibits significant low-rank behaviour like that seen in trailing vortex studies by Ranjan *et al.* (2022). This rank uniformity is more evident in the primary vortex system, which exists in the high-speed region of the outer wake.

The first three dominant POD modes of the P1 vortex pair at $x = 12$ are shown in figure 15(*a–c*), respectively. To aid in interpreting these results, an isocontour of time-averaged $\omega_x = 2$ is shown via the solid black line. PSD of the corresponding temporal coefficients is shown in figure 15(*d–f*), respectively. As was evident from figure 14(*a*), the first three modes have very similar energy levels, suggesting comparable contributions to the vortex dynamics. The dominant POD mode at $x = 12$ (figure 15*a*) clearly exhibits a dipole-like structure near the highly elliptic vortex core, indicative of a helical mode with azimuthal wavenumber $|m| = 1$. Consistent with the observations in Ranjan *et al.* (2020), this mode contributes to energy content in the range, $St \sim 0.1{-}0.3$ (figure 15*d*), characteristic of the short-wave elliptic instability (Kerswell 2002). The spectrum also displays a broadband character, as expected in the turbulent regions of the flow field. The second POD mode shown in figure 15(*b*) has an additional lobe within the core, which suggests the presence of higher helical modes in the primary vortex system. In addition to the helical mode frequencies, the associated spectrum (figure 15*e*) shows energy at $St \sim 0.03$ as well, which was earlier identified as the low-frequency breathing of the windward separation bubble, supporting the notion that low-frequency unsteadiness modulates the downstream vortex system. The third mode (figure 15*c*)

https://doi.org/10.1017/jfm.2026.12248 Published online by Cambridge University Press

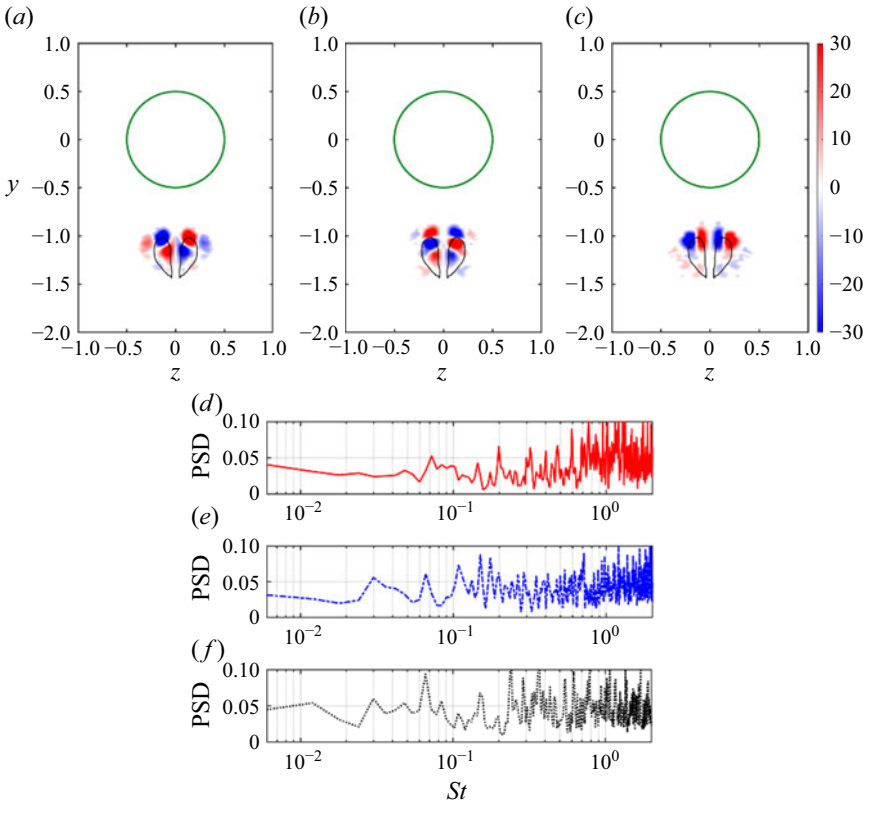


Figure 15. (*a–c*) First three POD modes of the P1 vortex pair and (*d–f*) PSD of the corresponding time coefficients at $x = 12$. The cylinder surface is marked by the green circle, while the isocontour line of time-averaged $\omega_x = 2$ is shown via the solid black line.

features a dipole structure predominantly located outside the mean vortex core, suggesting lateral oscillations of the vortex system, which also contributes to low-frequency dynamics as confirmed by its spectral content (figure 15*f*), with a prominent peak at $St \sim 0.07$.

The first three POD modes for the S1/T2 vortex pair and their corresponding spectra at $x = 12$ are shown in figures 16(*a–c*) and 16(*d–f*), respectively. The first two modes (figure 16*a*,*b*) present dipole structures within the elongated S1 vortex core, as expected from the helical mode, and their spectra (figure 16*d*,*e*) again show strong peaks in the $St \sim 0.1-0.3$ range. The third mode (figure 16*c*), in addition to the S1 dynamics, also represents additional fluctuations near the mean T2 vortex core, indicative of lateral movement of the T2 vortex pair. This is corroborated by its spectral content (figure 16*f*), which has peaks at $St \sim 0.07$ and $St \sim 0.1$, with the former aligning well with the lateral oscillation frequency of the primary vortex.

The above analysis underscores the ubiquitous nature of the low-frequency dynamics at $St \sim 0.03$ and 0.08, including within the windward separation and leeward wake/vortex system. To highlight the global dynamics of this low-frequency band, it is important to impose temporal coherence on the associated spatial mode due to the non-homogeneous variation of the basic state in the azimuthal direction. To this end, SPOD is performed on the 3-D computational domain spanning $5 \leqslant x \leqslant 15$, $-2.5 \leqslant y \leqslant 2.5$, $0 \leqslant z \leqslant 2.5$, to extract the 3-D spatial support of low-frequency components. Results are presented for

https://doi.org/10.1017/jfm.2026.12248 Published online by Cambridge University Press

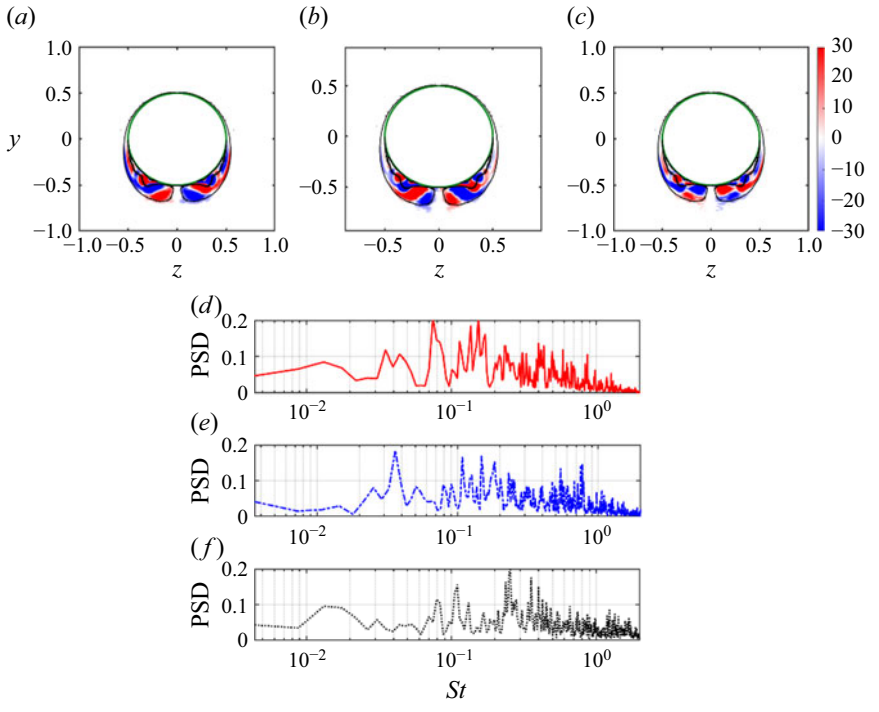


Figure 16. (*a–c*) First three POD modes of the S1/T2 vortex pair and (*d–f*) PSD of the corresponding time coefficients at $x = 12$. The cylinder surface is marked by the green circle, while the isocontour line of time-averaged $\omega_x = 2$ is shown via the solid black line.

two dominant components at $St \sim 0.03$ and 0.08 in figure 17, using the fluctuations of magnitude of the velocity field, $|\boldsymbol{v}| = \sqrt{u^2 + v^2 + w^2}$. It has to be noted that the SPOD analysis was performed on a single scalar $|\boldsymbol{v}|'$, calculated prior to the decomposition. Mean density gradient ($|\nabla\rho|$) contours are also included on the windward plane for contextual clarity.

Consistent with observations made in figure 12(*a*), the spatial support of $St \sim 0.03$ (shown in figure 17) on the windward plane highlights the separating shear layer and elongated streaks near the reattachment point with a phase switch, indicative of opposite directions of motion rooted in the growth and collapse of the bubble. These post-reattachment streaks (Bugeat *et al.* 2022) deflect away from the windward plane in the azimuthal direction due to the strong cross-flow generated downstream of the interaction. Additionally, this mode highlights the developing P1 and S1 vortex pairs as they wrap around the azimuth to the leeward plane. Post $x \sim 12$, the support within the detached primary vortex resembles a '*V*-shaped' inclined vertical motion symmetric about the leeward plane, consistent with the energetic structures identified on the streamwise plane in figure 15(*b*). The presence of this low frequency in the secondary/tertiary vortex system as well is confirmed by the near-wall long-wavelength structures. Similar inferences can be drawn from the mode at $St = 0.08$, in figure 17(*b*). It highlights large-scale oscillations of the P1 vortex core with significant lateral and vertical motions. This mode also highlights the S1 and T2 vortex pairs in the form of coherent shear-layer structures separating from the cylinder surface.

https://doi.org/10.1017/jfm.2026.12248 Published online by Cambridge University Press

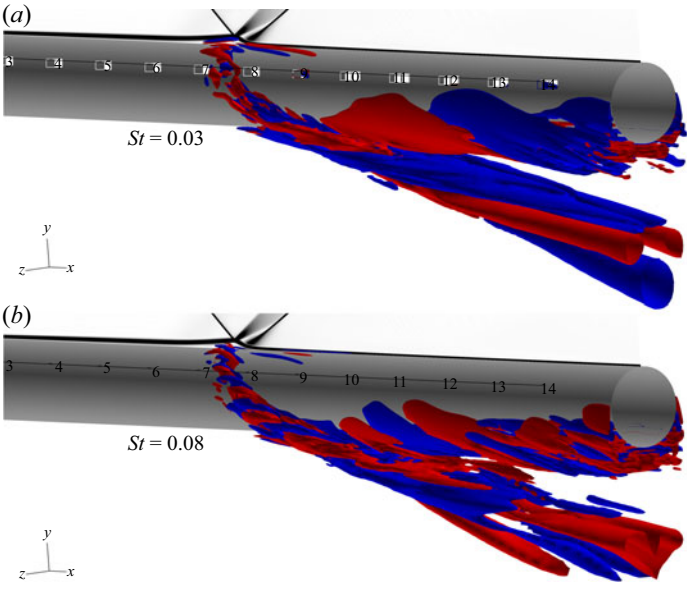


Figure 17. Dominant SPOD eigenmode of $|\boldsymbol{v}|$ at (*a*) $St = 0.03$ and (*b*) $St = 0.08$. Interaction of the windward plane is shown via contours of $|\nabla\rho|$.

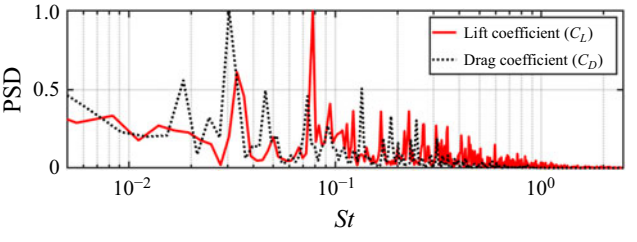


Figure 18. Normalised PSD of time-varying lift (C_L) and drag (C_D) coefficients.

The global 3-D nature of the dominant low-frequency dynamics in the axi-SWBLI identified above has a major influence on the unsteady aerodynamic loading on the surface. This can be observed in figure 18, which shows the normalised PSD of time-varying lift (C_L) and drag (C_D) coefficients. Here, lift and drag coefficients are calculated as follows:

$$C_L = \frac{L^*}{\frac{1}{2}\rho_\infty^* {u_\infty^*}^2 A^*} \quad C_D = \frac{D^*}{\frac{1}{2}\rho_\infty^* {u_\infty^*}^2 A^*}, \tag{7.2}$$

where, L^* and D^* are the lift and drag forces, and A^* is the surface area of the cylinder. The spectra of both force coefficients show a prominent dynamics occurring at a frequency of $St \sim 0.03$, and the spectrum of the lift coefficient shows an additional strong peak at $St = 0.08$, which was identified as the frequency of lateral motion of the vortices. This emphasises the significance of the low-frequency dynamics associated with the growth and collapse of the separation region and vortex-core oscillations in inducing unsteady surface loading on the cylinder.

https://doi.org/10.1017/jfm.2026.12248 Published online by Cambridge University Press

8. Conclusion

Flow features and the dynamics of an axi-SWBLI with $M_\infty = 2$ were examined in this study using implicit large-eddy simulations. Comparisons between reference experiments ($Re_D = 904\,745$) and current simulations demonstrated that the predictions increasingly aligned with experimental results as the Reynolds number and the state of the incoming BL approached the experimental conditions. The interaction at $Re_D = 35\,800$ was chosen for detailed analysis.

The axi-SWBLI generated highly 3-D flow features as follows. Near the interaction zone, three distinct sets of vortices were observed: a primary-first vortex (P1) that detaches from the surface, a secondary-first (S1) vortex pair in proximity to the cylinder and a weaker tertiary-first (T1) vortex pair that dissipates rapidly. Further downstream, secondary-second (S2) and tertiary-second vortices (T2) were observed, which were induced by the P1 vortex pair and eventually the detached S1 vortex pair. Surface streamlines revealed the imprint of these separation regions, highlighting areas of flow reversal and the locations of saddle points and source nodes at the mean separation and reattachment points, respectively. Change in the free-stream properties downstream of the impinging shock induced an effective negative angle of attack with respect to the cylinder, resulting in strong cross-flow away from the windward plane. A cross-flow away from the leeward plane was also observed due to the pressure gradient between the wake and the secondary vortex pair. These flow features significantly impact the aerodynamic loading experienced by the cylinder, as demonstrated by the pressure coefficient, which showed increased pressure in the wake and near the reattachment shock. The skin friction coefficient also highlighted the cross-flow-induced enlargement of the separation region from the windward to the leeward side and the presence of high skin friction streaks induced by the counter-rotating nature of the adjacent T1/S1 and T2/S2 vortices.

A TKE budget analysis was performed to understand the mechanisms driving turbulence generation in the interaction. The windward plane ($\phi = 0°$) exhibited peak TKE in the recirculation region and the spreading shear layer, with production driven by strong velocity fluctuations and gradients. Following shock impingement, production shifted to mechanisms involving vertical velocity gradients and Reynolds stress interactions. The mid-plane ($\phi = 90°$) showed peak TKE in the separating shear layer and vortex core, where shear production dominated. The leeward plane ($\phi = 180°$) experienced the highest TKE levels, with turbulence growth driven by turbulent transport.

Spectral and modal analyses yielded several insights into the temporal unsteadiness in this non-homogeneous interaction, as summarised below:

(i) St, $St_L \leqslant 0.03, 0.04$: very-low-frequency band linked to the 'breathing' motion of the separation bubble, characterised by growth and collapse of the bubble;
(ii) $0.03, 0.04 \leqslant St$, $St_L \leqslant 0.11, 0.15$: low-frequency band associated with 'flapping' motion of the reattaching shear layer, characterised by a wavering motion of the shear layer near the reattachment point;
(iii) $0.11, 0.15 \leqslant St$, $St_L \leqslant 1.5, 2$: mid-frequency band, the lower end of which shows large-scale shedding from the shear layer, while the higher end corresponds to $St_\theta \sim 0.012$, which is the K-H instability;
(iv) St, $St_L \geqslant 2, 2.5$: high-frequency band linked to convection of fine-scale turbulence in the reattached BL.

Dynamics of the prominent vortex systems generated from the interaction was studied using spectra extracted from their cores. They revealed stronger unsteadiness in the

https://doi.org/10.1017/jfm.2026.12248 Published online by Cambridge University Press

	n_x	n_{y_n}	n_ϕ	$(\Delta x^+)_{min}$	$(\Delta y_n^+)_{min}$	$(\Delta \phi^+)_{min}$
Baseline	1501	401	225	5	0.45	7
Fine	1501	575	301	5	0.25	5

Table 2. Parameters of grids used to perform convergence study.

secondary vortex, likely due to its proximity to the cylinder surface and the wake. Both the primary and secondary vortices exhibited low-frequency unsteadiness around $St \sim 0.03-0.04$, aligning with the bubble breathing frequency. A POD analysis showed that both the primary-first (P1) and secondary-first/tertiary-second (S1/T2) vortex systems exhibit broadband energy distribution across the leading energetic modes, lacking the low-rank structure typical of canonical trailing vortices. The dominant modes display signatures of short-wave elliptic instabilities ($St \sim 0.1-0.3$), and prominent low-frequency content at $St \sim 0.03$ and $St \sim 0.07-0.08$, which are linked to large-scale lateral oscillations and modulation by the upstream separation dynamics. A global analysis revealed that these frequencies are omnipresent in the interaction and wake regions and manifest as coherent structures spanning the windward shear layer, reattachment region and downstream vortex systems. In particular, the $St = 0.03$ mode captures azimuthally deflected reattachment streaks and an inclined 'V-shaped' oscillation in the detached P1 vortex, while the $St = 0.08$ mode reflects lateral and vertical vortex oscillations, including coherent shear-layer features within S1 and T2. These global low-frequency modes play a pivotal role in tailoring the unsteady surface pressure loading, as confirmed by the lift and drag spectra.

Acknowledgements. The authors would like to express their gratitude towards Professor R. Kumar for providing experimental visualisations and Ms G. Dashora for insightful discussions. Computations were performed at the Research Computing Center, Florida State University, and with a grant of computer time from the DoD HPCMP.

Funding. This research was supported by the Office of Naval Research through grant number N00014-24-1-2031, monitored by Dr L. Myers.

Declaration of interests. The authors report no conflict of interest.

Appendix: Grid convergence study

To ensure the flow features and the dynamics observed in the simulations have minimal dependence on grid parameters, a convergence study is performed, and key results are presented here. In addition to the grid discussed in § 2 (which will be referred to as the 'baseline grid'), computations at identical conditions were repeated on a 'fine grid', consisting of $\sim 260 \times 10^6$ nodes. While the number of nodes in the streamwise direction was maintained at 1501, 575 nodes were used to discretise the domain in the wall-normal direction, and 301 nodes were used along the azimuthal direction in the fine grid. The near-wall regions are resolved using a minimum wall-normal spacing of 5×10^{-4} in the fine grid (which is half the grid spacing used in the baseline grid). Other grid parameters are listed in table 2.

Figure 19(a) compares the streamwise variation of the wall skin friction coefficient at 5 equally spaced azimuthal locations around the cylinder from the baseline (solid line) and fine (dash-dot line) grids. The mean separation and reattachment points at all locations align closely between the two grids. The mean loading experienced by the surface is also identical between the two cases.

https://doi.org/10.1017/jfm.2026.12248 Published online by Cambridge University Press

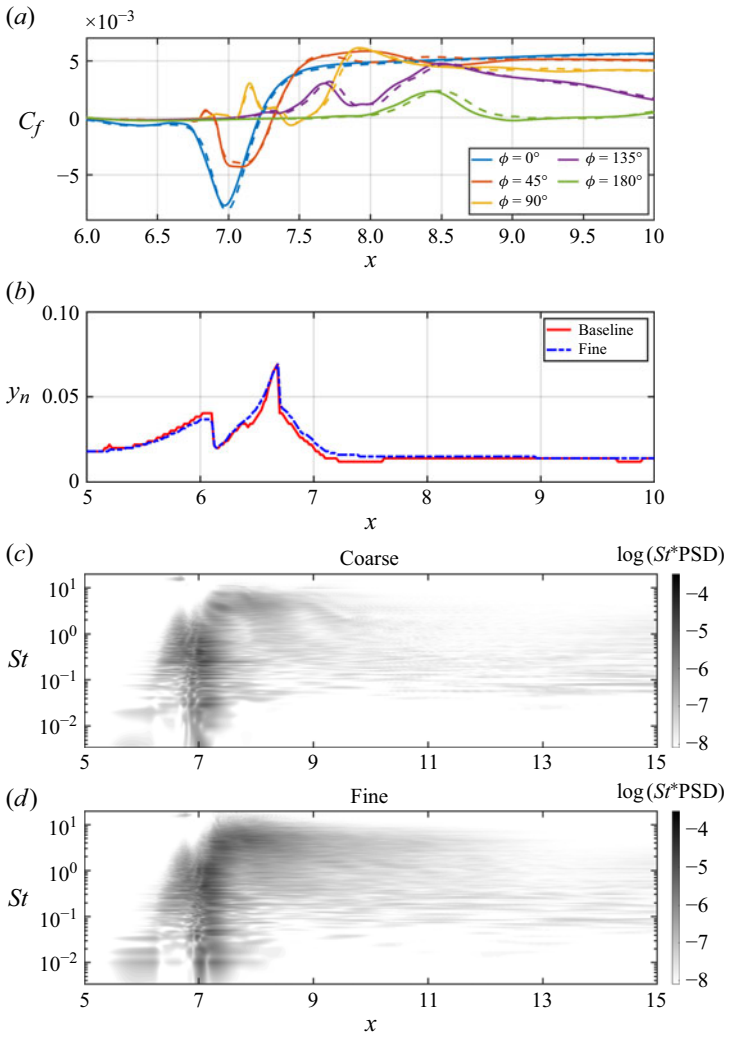


Figure 19. (*a*) Comparison of streamwise variation of wall skin friction coefficient at 5 azimuthal locations around the cylinder. Solid lines are used to show results from the baseline grid, while dash-dot lines are used to show results from the fine grid. (*b*) Comparison of streamwise distribution of wall-normal location at which peak TKE (fluctuation energy) levels are observed on the windward plane ($\phi = 0°$). (*c*,*d*) Comparison of streamwise variation of pre-multiplied wall pressure spectra on the windward plane ($\phi = 0°$) between the baseline and fine grids, respectively.

The streamwise variation of wall-normal location where peak TKE (fluctuation energy) levels exist on the windward plane ($\phi = 0°$) is plotted in figure 19(*b*), as obtained from the two grids. Consistent with figure 9(*a*), the wall-normal location of peak TKE levels increases in the detaching shear layer as the separation bubble grows. A peak distance of $y_n \sim 0.075$ is observed at the location of shock impingement, downstream of which it decreases as the shear layer reattaches.

Figures 19(*c*) and 19(*d*) compare the unsteady features predicted on the two grids. The streamwise variation of pre-multiplied wall pressure spectra at the $\phi = 0$ plane is presented. Very-low-frequency unsteadiness from the bubble breathing motion, a low-frequency dynamics associated with shear-layer flapping and a mid-frequency dynamics

https://doi.org/10.1017/jfm.2026.12248 Published online by Cambridge University Press

associated with K-H shedding from the shear layer match very well between the two grids. Some differences are observed in the high-frequency band post-reattachment, where the energy content is relatively lower. Overall, the mean flow features, statistics and dynamics are predicted by both grids consistently.

References

ADAMSON JR., T.C. & MESSITER, A.F. 1980 Analysis of two-dimensional interactions between shock waves and boundary layers. *Annu. Rev. Fluid Mech.* **12** (1), 103–138.

ADLER, M.C. & GAITONDE, D.V. 2018 Dynamic linear response of a shock/turbulent-boundary-layer interaction using constrained perturbations. *J. Fluid Mech.* **840**, 291–341.

ADLER, M.C. & GAITONDE, D.V. 2019 Flow similarity in strong swept-shock/turbulent-boundary-layer interactions. *AIAA J.* **57** (4), 1579–1593.

ADLER, M.C., GONZALEZ, D.R., STACK, C.M. & GAITONDE, D.V. 2018 Synthetic generation of equilibrium boundary layer turbulence from modeled statistics. *Comput. Fluids* **165**, 127–143.

AGOSTINI, L., LARCHEVÊQUE, L., DUPONT, P., DEBIÈVE, J.-F. & DUSSAUGE, J.-P. 2012 Zones of influence and shock motion in a shock/boundary-layer interaction. *AIAA J.* **50** (6), 1377–1387.

ANDREOPOULOS, Y., AGUI, J.H. & BRIASSULIS, G. 2000 Shock wave—turbulence interactions. *Annu. Rev. Fluid Mech.* **32** (1), 309–345.

ASWATHY NAIR, K. & UNNIKRISHNAN, S. 2024 Effects of nose bluntness on hypersonic transition over ogive-cylinder forebodies. *AIAA J.* **62** (2), 476–488.

BABINSKY, H. & HARVEY, J.K. 2011 *Shock Wave-Boundary-Layer Interactions*, vol. 32. Cambridge University Press.

BEAM, R. & WARMING, R. 1978 An implicit factored scheme for the compressible Navier–Stokes equations. *AIAA J.* **16** (4), 393–402.

BERKOOZ, G., HOLMES, P. & LUMLEY, J.L. 1993 The proper orthogonal decomposition in the analysis of turbulent flows. *Annu. Rev. Fluid Mech.* **25** (1), 539–575.

BHAGWANDIN, V.A. 2015 Numerical prediction of planar shock wave interaction with a cylindrical body. In *53rd AIAA Aerospace Sciences Meeting*.

BOGEY, C. 2022 Interactions between upstream-propagating guided jet waves and shear-layer instability waves near the nozzle of subsonic and nearly ideally expanded supersonic free jets with laminar boundary layers. *J. Fluid Mech.* **949**, A41.

BROSH, A., KUSSOY, M.I. & HUNG, C.M. 1985 Experimental and numerical investigation of a shock wave impingementon a cylinder. *AIAA J.* **23** (6), 840–846.

BUGEAT, B., ROBINET, J.-C., CHASSAING, J.-C. & SAGAUT, P. 2022 Low-frequency resolvent analysis of the laminar oblique shock wave/boundary layer interaction. *J. Fluid Mech.* **942**, A43.

CLEMENS, N.T. & NARAYANASWAMY, V. 2014 Low-frequency unsteadiness of shock wave/turbulent boundary layer interactions. *Annu. Rev. Fluid Mech.* **46** (1), 469–492.

CROW, S.C.J. 1970 Stability theory for a pair of trailing vortices. *AIAA J.* **8** (12), 2172–2179.

DÉLERY, J. & DUSSAUGE, J.-P. 2009 Some physical aspects of shock wave/boundary layer interactions. *Shock Waves* **19** (6), 453–468.

DOLLING, D.S. 2001 Fifty years of shock-wave/boundary-layer interaction research: what next? *AIAA J.* **39** (8), 1517–1531.

DUSSAUGE, J.-P., DUPONT, P. & DEBIÈVE, J.-F. 2006 Unsteadiness in shock wave boundary layer interactions with separation. *Aerosp. Sci. Technol.* **10** (2), 85–91.

DWIVEDI, A., SIDHARTH, G.S., NICHOLS, J.W., CANDLER, G.V. & JOVANOVIĆ, M.R. 2019 Reattachment streaks in hypersonic compression ramp flow: an input–output analysis. *J. Fluid Mech.* **880**, 113–135.

EAGLE, W.E. & DRISCOLL, J.F. 2014 Shock wave–boundary layer interactions in rectangular inlets: three-dimensional separation topology and critical points. *J. Fluid Mech.* **756**, 328–353.

FANG, J., ZHELTOVODOV, A.A., YAO, Y., MOULINEC, C. & EMERSON, D.R. 2020 On the turbulence amplification in shock-wave/turbulent boundary layer interaction. *J. Fluid Mech.* **897**, A32.

GAITONDE, D.V. 2015 Progress in shock wave/boundary layer interactions. *Prog. Aerosp. Sci.* **72**, 80–99.

GAITONDE, D.V. & ADLER, M.C. 2023 Dynamics of three-dimensional shock-wave/boundary-layer interactions. *Annu. Rev. Fluid Mech.* **55** (1), 291–321.

GAITONDE, D., SHANG, J.S. & EDWARDS, J.R. 1997 Structure of a supersonic three-dimensional cylinder/offset-flare turbulent interaction. *J. Spacecr. Rockets* **34** (3), 294–302.

GANAPATHISUBRAMANI, B., CLEMENS, N.T. & DOLLING, D.S. 2009 Low-frequency dynamics of shock-induced separation in a compression ramp interaction. *J. Fluid Mech.* **636**, 397–425.

https://doi.org/10.1017/jfm.2026.12248 Published online by Cambridge University Press

GARMANN, D.J. & VISBAL, M.R. 2019 High-fidelity simulations of afterbody vortex flows. *AIAA J.* **57** (9), 3980–3990.
GREEN, J.E. 1970 Interactions between shock waves and turbulent boundary layers. *Prog. Aerosp. Sci.* **11**, 235–340.
GREEN, S.I. & ACOSTA, A.J. 1991 Unsteady flow in trailing vortices. *J. Fluid Mech.* **227**, 107–134.
HADER, C. & FASEL, H.F. 2019 Direct numerical simulations of hypersonic boundary-layer transition for a flared cone: fundamental breakdown. *J. Fluid Mech.* **869**, 341–384.
HO, C.-M. & HUERRE, P. 1984 Perturbed free shear layers. *Annu. Rev. Fluid Mech.* **16**, 365–424.
HUNG, C.M. 1983 Impingement of an oblique shock wave on a cylinder. *J. Spacecr. Rockets* **20** (3), 201–206.
HUSSAIN, A.K.M.F. 1986 Coherent structures and turbulence. *J. Fluid Mech.* **173**, 303–356.
KERSWELL, R.R. 1999 Secondary instabilities in rapidly rotating fluids: inertial wave breakdown. *J. Fluid Mech.* **382**, 283–306.
KERSWELL, R.R. 2002 Elliptical instability. *Annu. Rev. Fluid Mech.* **34** (1), 83–113.
KHOBRAGADE, N., UNNIKRISHNAN, S. & KUMAR, R. 2022 Flow instabilities and impact of ramp–isolator junction on shock–boundary-layer interactions in a supersonic intake. *J. Fluid Mech.* **953**, A30.
KIYA, M. & SASAKI, K. 1983 Structure of a turbulent separation bubble. *J. Fluid Mech.* **137**, 83–113.
KUMAR, R., GUHA, T.K. & KUMAR, R. 2020 Role of secondary shear-layer vortices in the development of flow asymmetry on a cone–cylinder body at high angles of incidence. *Exp. Fluids* **61**, 1–20.
LAKSHMI NARASIMHA PRASAD, A., CHOKSHI, N. & UNNIKRISHNAN, S. 2025*a* Dynamics of axisymmetric shockwave-boundary layer interactions. In *AIAA AVIATION FORUM AND ASCEND 2025*, p. 3826.
LAKSHMI NARASIMHA PRASAD, A., SARATH, K.P. & UNNIKRISHNAN, S. 2025*b* Influence of free stream disturbance on hypersonic boundary layer dynamics over a cone–cylinder–flare. *J. Fluid Mech.* **1016**, A55.
LAKSHMI NARASIMHA PRASAD, A. & UNNIKRISHNAN, S. 2023 Effect of plasma actuator-based control on flow-field and acoustics of supersonic rectangular jets. *J. Fluid Mech.* **964**, A11.
LAKSHMI NARASIMHA PRASAD, A. & UNNIKRISHNAN, S. 2024 Noise mitigation in rectangular jets through plasma actuator-based shear layer control. *J. Fluid Mech.* **979**, A16.
LEWEKE, T., LE DIZÈS, S. & WILLIAMSON, C.H.K. 2016 Dynamics and instabilities of vortex pairs. *Annu. Rev. Fluid Mech.* **48** (1), 507–541.
LIU, X.-D., OSHER, S. & CHAN, T. 1994 Weighted essentially non-oscillatory schemes. *J. Comput. Phys.* **115** (1), 200–212.
MALMIR, F., DI LABBIO, G., LE FLOC'H, A., DUFRESNE, L., WEISS, J. & VÉTEL, J. 2024 Low-frequency unsteadiness in laminar separation bubbles. *J. Fluid Mech.* **999**, A99.
MASON, F., NATARAJAN, K. & KUMAR, R. 2021 Shock-wave/boundary-layer interactions on an axisymmetric body at mach 2. *AIAA J.* **59** (11), 4530–4543.
MICHALKE, A. 1965 On spatially growing disturbances in an inviscid shear layer. *J. Fluid Mech.* **23** (3), 521–544.
MOORE, D.W. & SAFFMAN, P.G. 1975 The instability of a straight vortex filament in a strain field. *Proc. R. Soc. Lond. A Math. Phys. Sci.* **346** (1646), 413–425.
NICHOLS, J.W., LARSSON, J., BERNARDINI, M. & PIROZZOLI, S. 2017 Stability and modal analysis of shock/boundary layer interactions. *J. Theor. Comput. Fluid Dyn.* **31**, 33–50.
PANARAS, A.G. 1996 Review of the physics of swept-shock/boundary layer interactions. *Prog. Aerosp. Sci.* **32** (2-3), 173–244.
PERRY, A.E. & CHONG, M.S. 1987 A description of eddying motions and flow patterns using critical-point concepts. *Annu. Rev. Fluid Mech.* **19**, 125–155.
PIPONNIAU, S., DUSSAUGE, J.-P., DEBIEVE, J.-F. & DUPONT, P. 2009 A simple model for low-frequency unsteadiness in shock-induced separation. *J. Fluid Mech.* **629**, 87–108.
PIROZZOLI, S. & GRASSO, F. 2006 Direct numerical simulation of impinging shock wave/turbulent boundary layer interaction at M = 2.25. *Phys. Fluids* **18** (6), 065113.
POGGIE, J., BISEK, N.J., KIMMEL, R.L. & STANFIELD, S.A. 2015 Spectral characteristics of separation shock unsteadiness. *AIAA J.* **53** (1), 200–214.
PULLIAM, T.H. & CHAUSSEE, D.S. 1981 A diagonal form of an implicit approximate-factorization algorithm. *J. Comput. Phys.* **39** (2), 347–363.
RANJAN, R., ROBINET, J.C. & GAITONDE, D.V. 2020 Meandering dynamics of streamwise vortex pairs in afterbody wakes. arXiv:2012.15444.
RANJAN, R., ROBINET, J.-C. & GAITONDE, D. 2022 Instability mechanisms in meandering streamwise vortex pairs of upswept afterbody wakes. *Eur. J. Mech. (B/ Fluids)* **96**, 90–104.
ROBINET, J.-C. 2007 Bifurcations in shock-wave/laminar-boundary-layer interaction: global instability approach. *J. Fluid Mech.* **579**, 85–112.

https://doi.org/10.1017/jfm.2026.12248 Published online by Cambridge University Press

RODRIGUEZ, D. & THEOFILIS, V. 2010 Structural changes of laminar separation bubbles induced by global linear instability. *J. Fluid Mech.* **655**, 280–305.
ROE, P.L. 1981 Approximate Riemann solvers, parameter vectors and difference schemes. *J. Comput. Phys.* **43**, 357–372.
SABNIS, K. & BABINSKY, H. 2023 A review of three-dimensional shock wave–boundary-layer interactions. *Progress in Aerospace Sciences* p. 100953.
SANDHAM, N.D. 2016 Effects of compressibility and shock-wave interactions on turbulent shear flows. *Flow Turbul. Combust.* **97**, 1–25.
SANSICA, A., SANDHAM, N.D. & HU, Z. 2016 Instability and low-frequency unsteadiness in a shock-induced laminar separation bubble. *J. Fluid Mech.* **798**, 5–26.
SARATH, K.P. & MANU, K.V. 2023 The onset of turbulence in decelerating diverging channel flows. *J. Fluid Mech.* **962**, A30.
SCHANDERL, W., JENSSEN, U., STROBL, C. & MANHART, M. 2017 The structure and budget of turbulent kinetic energy in front of a wall-mounted cylinder. *J. Fluid Mech.* **827**, 285–321.
SCHMID, P.J. & SIPP, D. 2016 Linear control of oscillator and amplifier flows. *Phys. Rev. Fluids* **1** (4), 040501.
SCHMIDT, O.T. & COLONIUS, T. 2020 Guide to spectral proper orthogonal decomposition. *AIAA J.* **58** (3), 1023–1033.
SCHÜLEIN, E. 2006 Skin friction and heat flux measurements in shock/boundary layer interaction flows. *AIAA J.* **44** (8), 1732–1741.
SEÇKIN, S., MEARS, L.J., SONG, M.J., ALVI, F.S. & ZIGUNOV, F. 2023 Surface properties of double-fin generated shock-wave/boundary-layer interactions. *AIAA J.* **61** (12), 5302–5319.
SETTLES, G.S. & TENG, H.-Y. 1984 Cylindrical and conical flow regimes of three-dimensional shock/boundary-layer interactions. *AIAA J.* **22** (2), 194–200.
SHAHRIAR, A., KUMAR, R. & SHOELE, K. 2023 Vortex dynamics of axisymmetric cones at high angles of attack. *J. Theor. Comput. Fluid Dyn.* **37** (3), 337–356.
SIMONI, D., LENGANI, D., UBALDI, M., ZUNINO, P./ & DELLACASAGRANDE, M. 2017 Inspection of the dynamic properties of laminar separation bubbles: free-stream turbulence intensity effects for different reynolds numbers. *Exp. Fluids* **58**, 1–14.
STEPHEN, E.J., FARNSWORTH, J.A., PORTER, C.O., DECKER, R., MCLAUGHLIN, T.E. & DUDLEY, J.G. 2013 Impinging shock wave-boundary layer interactions on a three-dimensional body. In *43rd AIAA Fluid Dynamics Conference*.
TOBAK, M. & PEAKE, D.J. 1981 Topology of three-dimensional separated flows. *Tech. Rep*. A-8554. NASA.
TOUBER, E. & SANDHAM, N.D. 2009 Large-eddy simulation of low-frequency unsteadiness in a turbulent shock-induced separation bubble. *J. Theor. Comput. Fluid Dyn.* **23**, 79–107.
TOWNE, A., SCHMIDT, O.T. & COLONIUS, T. 2018 Spectral proper orthogonal decomposition and its relationship to dynamic mode decomposition and resolvent analysis. *J. Fluid Mech.* **847**, 821–867.
TSAI, C.-Y. & WIDNALL, S.E. 1976 The stability of short waves on a straight vortex filament in a weak externally imposed strain field. *J. Fluid Mech.* **73** (4), 721–733.
WAHIDI, R., CHIN, H., HE, S., ADLER, M.C. & KUMAR, R. 2024 Experimental/computational investigation of shock-wave/boundary-layer interaction on an axisymmetric cone. In *AIAA AVIATION FORUM AND ASCEND 2024*, p. 3718.
XU, S., WANG, Y., WANG, Z., FAN, X. & XIONG, B. 2022 Unsteady behavior of hypersonic inlet unstart caused by high angle of attack. *Aerosp. Sci. Technol.* **130**, 107884.
ZIGUNOV, F., SELLAPPAN, P. & ALVI, F.S. 2020 Dynamics of the slanted cylinder afterbody vortices. In *AIAA Scitech 2020 Forum*, p. 1322.
ZUO, F.-Y. & PIROZZOLI, S. 2024 Recent progress in conical shock wave/boundary layer interaction with spanwise pressure gradient. *Propul. Power Res.* **13** (3), 295–318.

https://doi.org/10.1017/jfm.2026.12248 Published online by Cambridge University Press